SANDIA REPORT
SAND2023-14433
Printed November 2023

Sandia National Laboratories

Infrasound Detections of Low-Magnitude Earthquakes: Preliminary Results of the West Texas Acoustic Experiment

Loring Schaible,
Fransiska Dannemann Dugick,
Daniel C. Bowman

Prepared by
Sandia National Laboratories
Albuquerque, New Mexico
87185 and Livermore,
California 94550

Issued by Sandia National Laboratories, operated for the United States Department of Energy by National Technology & Engineering Solutions of Sandia, LLC.

Available to DOE and DOE contractors from
U.S. Department of Energy
Office of Scientific and Technical Information
P.O. Box 62
Oak Ridge, TN 37831

Telephone: (865) 576-8401
Facsimile: (865) 576-5728
E-Mail: reports@osti.gov
Online ordering: http://www.osti.gov/scitech

Available to the public from
U.S. Department of Commerce
National Technical Information Service
5301 Shawnee Rd
Alexandria, VA 22312

Telephone: (800) 553-6847
Facsimile: (703) 605-6900
E-Mail: orders@ntis.gov
Online order: https://classic.ntis.gov/help/order-methods/

ABSTRACT

Infrasound observations have grown increasingly important for the monitoring of earthquakes. While large earthquakes generate infrasound that can be detected thousands of kilometers away, there are few near-field observations of infrasound generated by low-magnitude events. We describe preliminary results of the West Texas Acoustic Experiment, during which infrasound sensors collected continuous data in the Permian Basin for a six-month period spanning January—June 2023. During this time, more than 1000 earthquakes with magnitudes between 1.2 and 4.2 occurred within 50 km of the network. We used spectral analysis, array processing, and manual inspection of waveforms to evaluate arrivals of infrasound signals following 84 events with magnitudes between 2.5 and 4.2. Here, we describe eight such events and the infrasound signals associated with each. We find detections of seismic-to-acoustic infrasound signals associated with seven events. We also find strong evidence of a laterally-propagating, purely acoustic wave generated by an M2.9 earthquake.

ACKNOWLEDGEMENTS

This Source Physics Experiment (SPE) research was funded by the National Nuclear Security Administration, Defense Nuclear Nonproliferation Research and Development (NNSA DNN R&D). The authors acknowledge important interdisciplinary collaboration with scientists and engineers from Los Alamos National Laboratory (LANL), Lawrence Livermore National Laboratory (LLNL), the Nevada National Security Site (NNSS), Sandia National Laboratories (SNL), and the University of Nevada, Reno (UNR).

Michael Fleigle, SNL Department 06752 coordinated and led the field deployment detailed in this report. Nora Wynn assisted with the field deployments.

Permission for land access and equipment deployment was granted by University Lands through the University of Texas at Austin. The authors acknowledge Alexandros Savvaidis and Cooper McCabe from the Bureau of Economic Geology, University of Texas at Austin for assistance with coordinating and executing the field campaign detailed in this report.

CONTENTS

LIST OF FIGURES

LIST OF TABLES

This page left blank

ACRONYMS AND TERMS

Acronym/Term	Definition
EIS	epicentral infrasound
LIS	local infrasound
SIS	secondary infrasound
SNR	signal-to-noise ratio
Pa	Pascals
TexNet	Texas Seismological Network and Seismology Research
USGS	United States Geological Survey

1. INTRODUCTION

Humans experience compressional waves traveling through the atmosphere with frequencies from ~20 Hz to 20 kHz as audible sound. Infrasound waves are comprised of frequencies below ('infra') the nominal human hearing threshold of ~20 Hz. Infrasound pressure fluctuations can be recorded by microbarometers and microphones.

Infrasound can be generated by anthropogenic events such as explosions (e.g., Bowman & Krishnamoorthy, 2021; Walker *et al.,* 2011, Koch & Pilger, 2019) and natural sources such as shallow earthquakes (Arrrowsmith *et al.,* 2012; Johnson *et al.,* 2020). Earthquake infrasound is caused by low-frequency vertical ground motion near the epicenter and elsewhere that creates atmospheric pressure fluctuations (Johnson *et al.,* 2020; Mutschlecner & Whitaker, 2005; Wilson *et al.,* 2023; Lamb *et al.,* 2021). Earthquakes also produce audible sounds in the frequency range ~20 to 70 Hz (Lamb *et al.,* 2021). However, for simplicity, herein we refer earthquake infrasound as inclusive of both the inaudible (<~20 Hz) and audible (~20–70 Hz) atmospheric pressure waves generated by earthquake-induced ground motion.

1.1. Earthquake Infrasound

Earthquakes generate infrasound in three ways (Arrowsmith *et al.,* 2010). Epicentral infrasound (EIS) is generated at the epicenter due to vertical epicentral ground motion (Whitaker *et al.,* 2003) and propagates laterally away from the epicenter as an acoustic wave. EIS arrives at receivers at acoustic velocities. The nominal speed of sound is about 0.340 km/s, but infrasound travel speeds can range from 0.250–0.425 km/s (Negraru *et al.,* 2010). Local infrasound (LIS) is an acoustic wave generated by the ground-to-air coupling of seismic waves across the Earth/atmosphere interface near the receiver, signals from the vertical displacement of the sensor through the atmospheric pressure gradient, and/or spurious signals generated by the instrument's sensitivity to ground motion. LIS therefore arrives at receivers at seismic velocities. The third form of earthquake infrasound is secondary infrasound (SIS), a combination of EIS and LIS. Seismic waves emanating away from an earthquake can cause vertical ground motion at a location other than the receiver, creating an infrasound wave. This wave then travels to the receiver at acoustic velocities. The apparent velocity of the arriving wave, calculated relative to the earthquake origin time, is intermediate between seismic and acoustic values. In keeping with existing convention, LIS is known as a seismic arrival of infrasound while EIS and SIS are considered purely acoustic arrivals (Arrowsmith *et al.,* 2010).

Many detections of earthquake generated infrasound occur at distances greater than 150 km and up to several thousand km from the source (e.g., Le Pichon *et al.,* 2006; Mutschlecner & Whitaker, 2005). In such instances, EIS and SIS arrive at receivers after refracting through the atmosphere. For example, EIS generated during the 1964 Great Alaskan earthquake was detected in Berkeley, California (Bolt, 1964). Three infrasound stations detected SIS radiated by the Andes mountains at epicentral distances of 410–2300 km (Le Pichon *et al.,* 2006). LIS signals can also be detected at great distances, caused by the arrival of seismic phases through the solid earth. Seismic waves originating from the 1959 M7.2 Hebgen Lake earthquake in Montana generated an LIS signal recorded in Washington, DC (Cook, 1971).

The subject of this study, however, is detections of infrasound generated by low-magnitude earthquakes within 50 km of receivers. Of particular interest are detections of laterally propagating EIS signals which, when detected proximally, have traveled entirely in the troposphere, directly from source to receiver. Of secondary interest are detections of LIS.

Wilson *et al.* (2023) conducted a study like the one described in this paper, searching for infrasound arrivals associated with 360 low-magnitude earthquakes within 50 km of three different

infrasound arrays. The largest event had a magnitude of 4.2 but most of the events had magnitudes less than 2.0. They detected LIS arrivals associated with several earthquakes. For example, an M4.1 in southern Nevada created a broadband 1–30 Hz LIS signal arrival, recorded on an array 5.5 km away (Wilson *et al.,* 2023). Another M2.2 event about 15 km away also generated detectable LIS (Wilson *et al.,* 2023). LIS has been observed in other studies for several near-field, low-magnitude earthquakes. An M3.6 event in Czech Republic produced a 1–12 Hz LIS signal that was recorded on two instruments within 7 km (Laštovička *et al.,* 2010). An M3.6 event in Idaho generated an LIS signal on multiple receivers within 25 km from the hypocenter (Johnson *et al.,* 2020). The lowest magnitude earthquake yet observed via LIS originated from an anthropogenically induced M1.87 earthquake in Finland (Lamb *et al.,* 2021). Two instruments within 8 km of the epicenter recorded a broadband 15–45 Hz acoustic signal. These are the first observations of an acoustic signal of an induced earthquake (Lamb *et al.,* 2021). This is additionally the lowest magnitude event to be recorded with acoustic instrumentation (Lamb *et al.,* 2021).

To date, there are no publications of laterally propagating EIS observed at proximal distances. For example, Wilson *et al.* (2023) found no arrivals of EIS associated with any of the 360 events occurring <50 km from receivers. The closest approximation of such an observation was made by Johnson *et al.,* (2023), during which LIS and SIS were observed following an ML3.5 event in Idaho. The receiver was in the epicentral zone, 0.6±1 km from the epicenter, and therefore the signal interpreted as LIS may be that of EIS given that it is difficult to differentiate LIS from EIS when the receiver is in/near epicenter. Previous work by Whitaker *et al.* (2003) suggests that events below M5.0 may not create enough vertical displacement of the ground surface to generate detectable EIS signals. More research is needed to understand the generation of infrasound by low magnitude earthquakes and the conditions that benefit detection at nearby receivers. The West Texas Acoustic Experiment provides a unique opportunity to do so.

2. STUDY AREA

The Permian Basin of central Texas and southeastern New Mexico has produced hydrocarbons for more than 100 years (Energy Information Administration, 2020). With vast untapped reserves of oil and natural gas, the Permian Basin is one of the largest hydrocarbon-producing basins in the United States and the world (Energy Information Administration, 2017).

This study utilizes data recorded at seventeen infrasound instruments from three arrays that were deployed in the Delaware Basin near its western margin (Figure 1). The Delaware Basin extends from west Texas into southeastern NM and is one of the three main sub-basins of the Permian Basin.

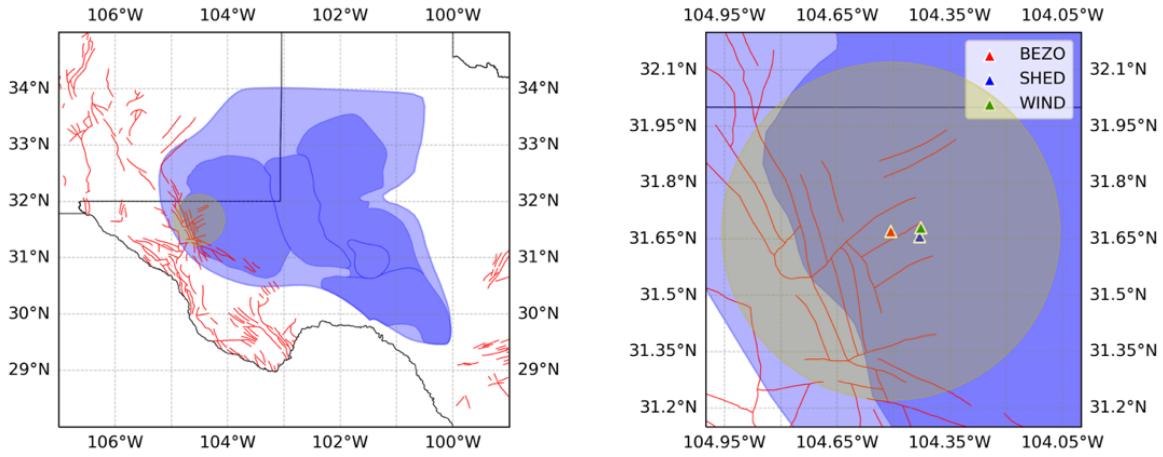

Figure 1. Left: Map of Permian Basin (in blue) with sub-basins (darker blue). The area of interest is a circle of 50 km radius centered on the arrays (yellow). Mapped faults (in red). The Delaware Basin is the one farthest west. Right: Approximate area of interest within 50 km of all three array centers. The whole area is in the Permian Basin and most is in the Delaware Basin.

Induced seismicity has become a subject of increasing concern in the Permian Basin, given the observed increase in seismic activity alongside the simultaneous growth of extractive industries. The number of earthquakes in the study area has increased steadily since 1999 from tens to thousands of earthquakes per year (Figure 2). Some of the seismic activity in the Delaware Basin is likely caused by hydraulic fracturing (Lomax & Savvaidis, 2019). Increased seismic instrumentation as part of the Texas Seismological Network and Seismology Research (TexNet) initiative has also improved the detection of small earthquakes. The magnitude of completeness, the minimum magnitude above which all earthquakes within a given region are reliably recorded, has decreased from 2.7 in west Texas to less than 1.5 in specific areas. The magnitude of completeness is 1.3 in the Delaware Basin (Savvaidis *et al.,* 2019). The area studied in this project was chosen because of the high seismic activity as well as the high detection reliability of small earthquakes.

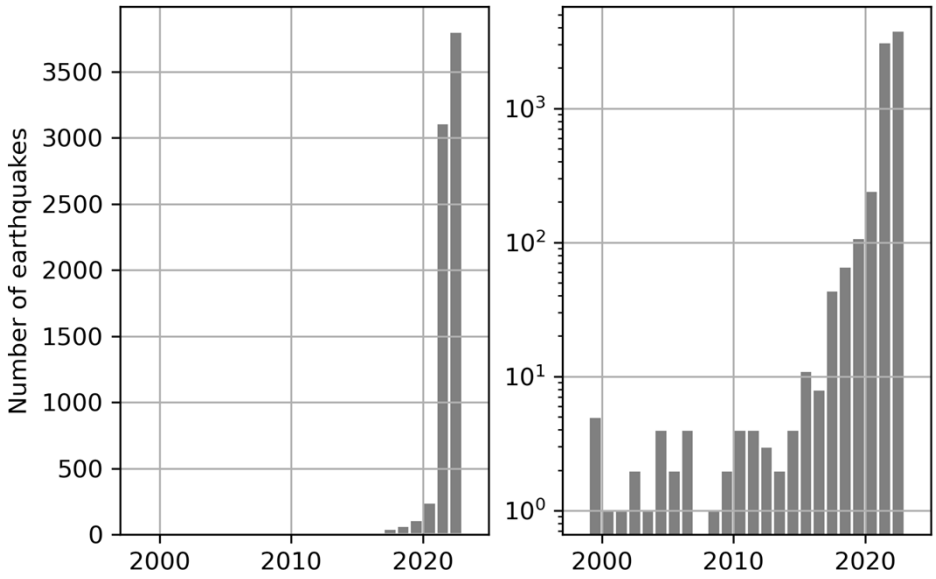

Figure 2. Number of earthquakes per year since 1999 in the area within 50 km of all three arrays. Linear scale on the left, logarithmic on the right. The x-axis denotes year. Data from 2007 is missing.

3. DATA

3.1. Infrasound Data

Seventeen infrasound instruments arranged in three separate arrays were deployed from January to June 2023. Instruments were deployed on January 8 and retrieved on June 22. Each array had a central element with five surrounding elements at an aperture of about 100 m (Figure 3). Instrument locations and recording types are summarized in Table 1. Instruments WIND.3 and SHED.6 were co-located with TexNet seismic stations PB36 and PB35, respectively. Some instruments were analog Hyperion microbarometers that were digitized on a RefTek 130S recorder. All other instruments were digital Hyperion microbarometers. The digital instruments are seismically decoupled, reducing their response to ground motion (Hyperion Technology Group, Inc). In other words, the seismically decoupled instruments should be less sensitive to the fraction of LIS that results from direct disturbance of the sensor. The analog instruments are not seismically decoupled. All instruments recorded at a 100 Hz sampling rate. The instruments have a flat response for the frequencies of interest (>1 Hz). Wind screens made from trampoline material were used for wind noise suppression at arrays BEZO and SHED. Wind screens made from metal were used for wind noise suppression at the WIND array. Arrays BEZO are SHED are ~7.4 km apart. Arrays BEZO and WIND are ~7.7 km apart. Arrays SHED and WIND are ~2.7 km apart.

Table 1. Instrument locations and recording types. Element 1 is the center in all three arrays.

Array	Element	Latitude	Longitude	Recording
BEZO	1	31.670515	-104.50709	Analog
	2	31.671301	-104.50687	Analog
	3	31.670105	-104.50634	Analog
	4	31.669674	-104.50717	Digital
	6	31.670862	-104.50792	Digital
SHED	1	31.656780	-104.43114	Analog
	2	31.657242	-104.43204	Analog
	3	31.657598	-104.43069	Analog
	4	31.656567	-104.43015	Digital
	5	31.655928	-104.43085	Digital
	6	31.656364	-104.43214	Digital
WIND	1	31.680456	-104.42700	Analog
	2	31.681236	-104.42704	Digital
	3	31.680315	-104.42587	Digital
	4	31.679502	-104.42696	Digital
	5	31.679808	-104.42772	Analog
	6	31.680531	-104.42796	Analog

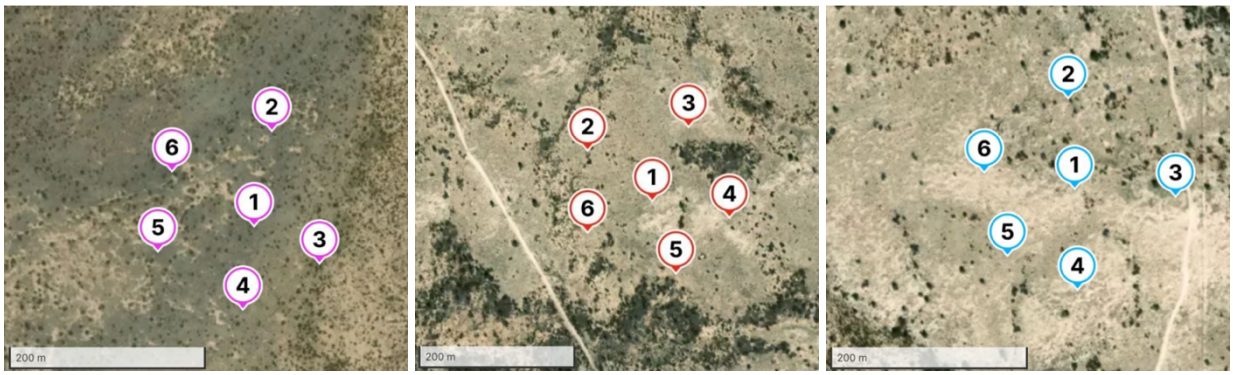

Figure 3. Geometries of the BEZO, SHED, and WIND arrays (left to right) Note that BEZO element 5 was not deployed.

3.2. Earthquake Catalog

The United States Geological Survey (USGS) catalog recorded 1077 earthquakes between January 9 and June 22, 2023, within 50 km of the centers of all three arrays (Figure 4). The smallest event was M1.2 and the largest M4.2. All events were less than 11 km deep (Figure 5).

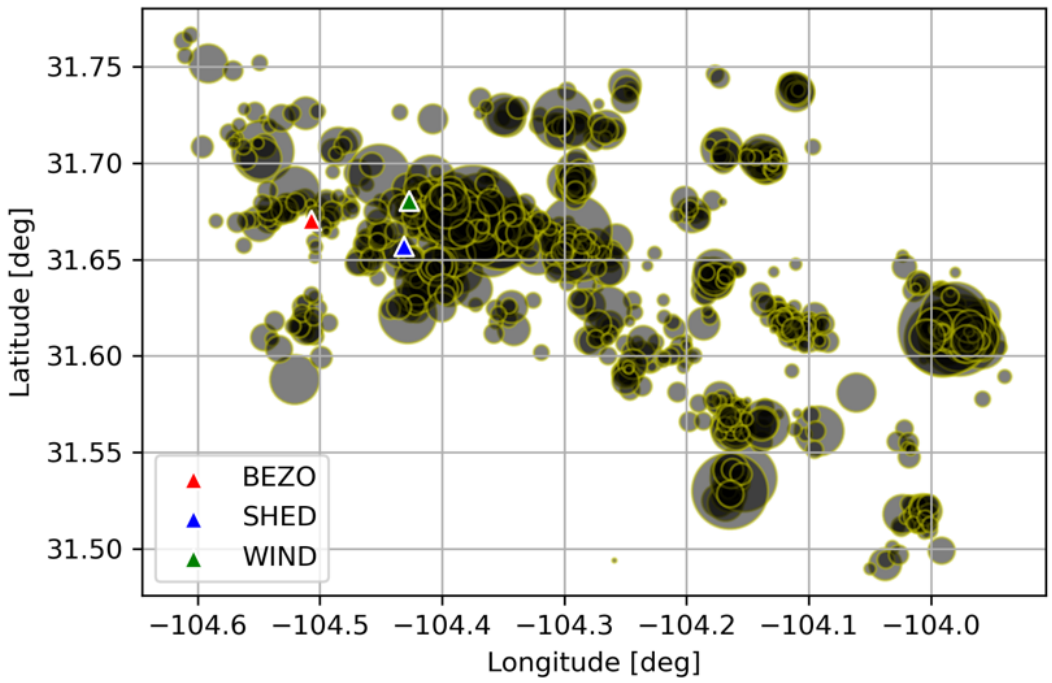

Figure 4. Spatial distribution of the 1077 earthquakes (size scaled by magnitude) recorded between January 9 and June 22, 2023.

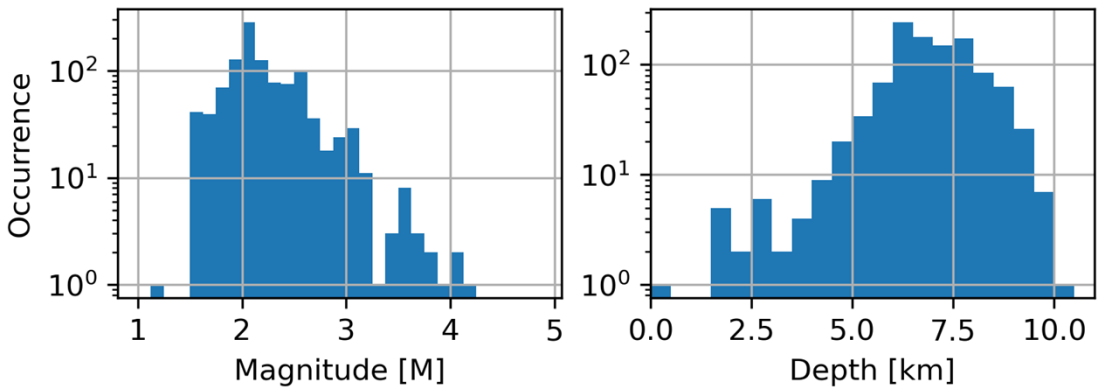

Figure 5. Semi-log distributions of earthquake magnitudes and depths.

4. METHODS

Following methodologies established in Wilson *et al.* (2023), we plotted waveforms and spectrograms for each earthquake M≥2.5 across all instruments. We then subsequently focused only on events for which there was data recorded on three or more elements of any single array. At the time of these analyses, only data from approximately the first half of the deployment were available. As such, we investigated 84 events with magnitudes between 2.5 and 4.2 occurring January 18 to March 26, 2023. We visually inspected each waveform and spectrogram for evidence of infrasound arrivals. We identified possible infrasound arrivals as concurrent waveform features and spectral content changes occurring within the expected range of arrivals, which is discussed later.

Unless otherwise stated, both waveforms and spectrograms are of 5–50 Hz bandpassed data. Narrower passbands were selected in specific situations. Previous studies show that proximal infrasound signals consist of broadband excitement across 1–60 Hz (Wilson *et al.*, 2023; Lamb *et al.,* 2021; Johnson *et al.,* 2023; Laštovička *et al.,* 2010; Sylvander *et al.,* 2007). The lower frequency limit of 5 Hz excludes the microbarom range of 0.1–0.4 Hz and masks other low-frequency noise (Johnson *et al.,* 2020; Wilson *et al.*, 2023; Bowman *et al.,* 2005). The upper limit of 50 Hz is the Nyquist frequency of our instruments, which was also used in Johnson *et al.* (2020).

Celerity is an apparent velocity of a wavefront assuming an origin time and location. In this case, the origin time is the reported time of the earthquake, and the location is the reported epicenter. Celerity calculations are simply the distance separating the epicenter and receiver divided by the time difference between the event and the arrival.

4.1. Travel Time Calculations

We calculated windows in which seismic and acoustic signals originating at each earthquake would arrive at each array. Compressional body waves, also known as P-waves, are seismic waves that travel through the Earth. P-waves are the first to arrive at any receiver following an event. A variety of seismic phases — such as surface waves that travel along the Earth's surface — would arrive following the P-waves. EIS waves would arrive after all seismic phases. Therefore, the span of time between predicted P-wave and EIS arrivals should include all possible seismic and infrasonic phases originating at the earthquake. The earliest and latest arrivals of P-waves and EIS at a receiver are determined by the earthquake's true location and the propagation velocities of the waves.

We define some spatial relationships between earthquake locations and receivers to calculate arrival times of seismic phases and infrasound. An earthquake has a reported depth, depth error (errZ), location (epicenter) and location error (errH) (refer to Figure 6). The earthquake's true hypocenter falls in a cylinder of height equal to 2*errZ and radius equal to 2*errH. The hypocentral location nearest to a given receiver is at depth-errZ and distance-errH. The hypocentral location farthest from a given receiver is at depth+errZ and distance+errH.

The arrival time of P-waves is governed by the velocity of such waves. P-wave velocities given the local geology are suggested to be as high as 5.0 km/s (Huang *et al.,* 2017) and as low as 3.5 km/s (Huang *et al.,* 2019). The earliest predicted arrival of a P-wave, therefore, would be for a 5 km/s wave originating at the location nearest to the receiver. Meanwhile, the latest arrival of a P-wave would be for a 3.5 km/s wave originating at the location farthest from the receiver. These two times define a P-wave arrival window. A signal in this window indicates the arrival of LIS, generated at or near the receiver by ground motion caused by the arriving P-wave.

The arrival time of EIS signals is likewise governed by the local acoustic velocity. We considered a range of possible acoustic velocities, ranging from 0.25–0.425 km/s (Negraru *et al.,* 2010). EIS is generated at the epicenter due to ground motion generated by seismic waves arriving at the surface. Therefore, the predicted arrival time of EIS at a receiver depends on both the travel time of the seismic waves through the earth and the travel time of the infrasound waves through the air. Therefore, the earliest predicted EIS arrival would occur with a 0.425 km/s sound wave traveling from the hypocenter nearest to the receiver, and associated P-waves traveling at 5 km/s from the shallowest hypocenter. The latest predicted EIS arrival would occur with a 0.25 km/s wave traveling from the epicenter farthest from the receiver, and associated P-waves traveling at 3.5 km/s from the deepest hypocenter. These calculations assume that infrasound travels in a straight line. The two times define an EIS arrival window. An infrasound arrival in this window suggests a signal that was generated at the epicenter and traveled to the receiver at the speed of sound. Seismic phases with velocities intermediate between those of P-wave and EIS may create LIS signals. For example, surface waves generated by earthquakes travel slower than P-waves. Therefore, a surface wave traveling away from the epicenter may move the ground near the receiver, creating a LIS signal.

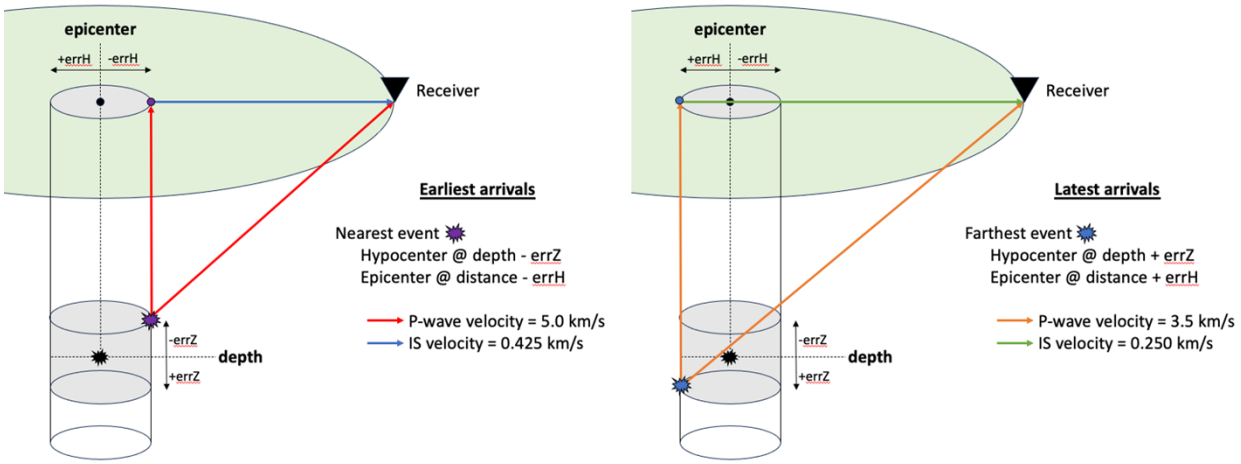

Figure 6. Nearest and farthest possible locations of an earthquake with epicentral (errH) and depth error (errZ).

4.2. Array Processing

We used a built-in tool in Obspy (obspy.signal.array_analysis.array_processing) to perform array processing (Beyreuther *et al.,* 2010). The user inputs waveforms of interest. The routine calculates the absolute power of the waveforms, which is a metric of coherence amongst the waveforms. The routine also calculates the back azimuth and slowness, the reciprocal of wave propagation velocity, of the coherent parts of the waveform. We performed the processing using a range of 0 to 4 s/km for slowness values, following Johnson *et al.* (2023). Using a wide range of slowness values allows for wave propagation velocities ranging from seismic values down to 0.25 km/s. Given that the slowness of infrasound varies from the nominal value of 3 s/km, a range up to 4 s/km can capture other realistic values that might be observed in the field (Johnson *et al.*, 2023).

We used array processing for two events: tx2023cauk and tx2023cayr. For each, we bandpassed the waveforms from 10–12 Hz, and used a window length of 1.5 seconds and a window fraction of 1/50th the window length.

5. RESULTS

Here we present the results of observed infrasound signals associated with eight earthquakes (Table 2). The eight events described here are associated with coherent infrasound signals recorded on three or more elements of at least one array. These eight events occurred between January 21 and February 24, 2023, with magnitudes ranging from M2.5 to M3.0. Source-receiver distances vary from 2.0 to 38.3 km.

Table 2. USGS Catalog earthquake IDs, origin times, magnitudes, and hypocentral location (latitude, longitude, depth) and location error (horizontal and vertical). The three rightmost columns indicate the distances from the epicenter to each of the array centers. Red text indicates that infrasound signals associated with this event were observed on this array and are featured in this paper.

ID	DT [UTC]	MAG	LAT	LON	ERR_H [km]	DEPTH [km]	ERR_Z [km]	BEZO [km]	SHED [km]	WIND [km]
tx2023blmu	2023-01-21 12:27:36.555	2.5	31.7234	-104.5313	1.4	6.0	0.7	6.3	12.0	11.0
tx2023bvwo	2023-01-27 04:47:14.290	2.9	31.7368	-104.1109	0.4	6.9	0.5	38.3	31.6	30.6
tx2023cauk	2023-01-29 21:22:27.763	2.7	31.6475	-104.4046	0.8	6.1	0.9	10.0	2.7	4.2
tx2023cayr	2023-01-29 23:31:49.407	2.9	31.6462	-104.4040	0.8	4.5	1.0	10.1	2.8	4.4
tx2023cbwa	2023-01-30 11:19:58.616	2.5	31.6276	-104.2860	0.7	7.6	0.9	21.5	14.1	14.6
tx2023cdzu	2023-01-31 15:30:02.861	2.5	31.6870	-104.4200	1.0	6.1	0.7	8.5	3.5	1.0
tx2023dafm	2023-02-12 19:23:17.172	3.0	31.6520	-104.3898	1.1	4.5	1.1	11.3	4.0	4.7
tx2023dvvu	2023-02-24 15:28:00.374	2.7	31.6806	-104.4059	1.1	5.7	1.3	9.7	3.6	2.0

For each event we show the following figures:

1) Waveform and spectrogram for each array element on which there is an infrasound arrival. Waveforms record changes in atmospheric pressure in Pascals (Pa) over time. Spectrograms display the frequency content the waveform as a function of time. The colors in the spectrograms have units of Pa/(Hz)^1/2 and are all scaled individually. On each plot, the yellow vertical line indicates the earthquake origin time. Vertical dashed black and white lines mark the bounds of the predicted P-wave arrival. The dotted red lines mark the bounds of the predicted arrival of an EIS wave.

2) Waveform of atmospheric pressure over a period of 1 hour centered on the event origin time. The duration highlighted in red is the same as that in the corresponding waveform and spectrogram figure immediately preceding. This plot provides an indication of the noise conditions at the instrument at the time of the event.

5.1. Event tx2023blmu

5.1.1. Results

An M2.5 earthquake with ID 'tx2023blmu' occurred on January 21, 2023, at 12:27:37 UTC at a depth of 6.0±0.7 km. Infrasound signals were observed at BEZO array elements 1, 2, 3, and 6. No infrasound signals were observed at any of the elements of either the SHED or WIND arrays. This earthquake occurred 6.3±1.4 km from the central element of the BEZO array. The SHED and WIND arrays were about twice as distant. As seen in Figure 7, instruments BEZO 1, 2, 3, and 6 each recorded a qualitatively high signal-to-noise ratio (SNR) atmospheric pressure change with amplitudes of ~0.4–1.0 Pa. The waveform is comprised of ~7–40 Hz energy with amplitudes much greater than background levels. Each signal arrived around 12:27:39, just after the predicted 3.5 km/s P-wave arrival time. As seen in Figure 8, each of these arrivals have amplitudes much greater than that of background noise.

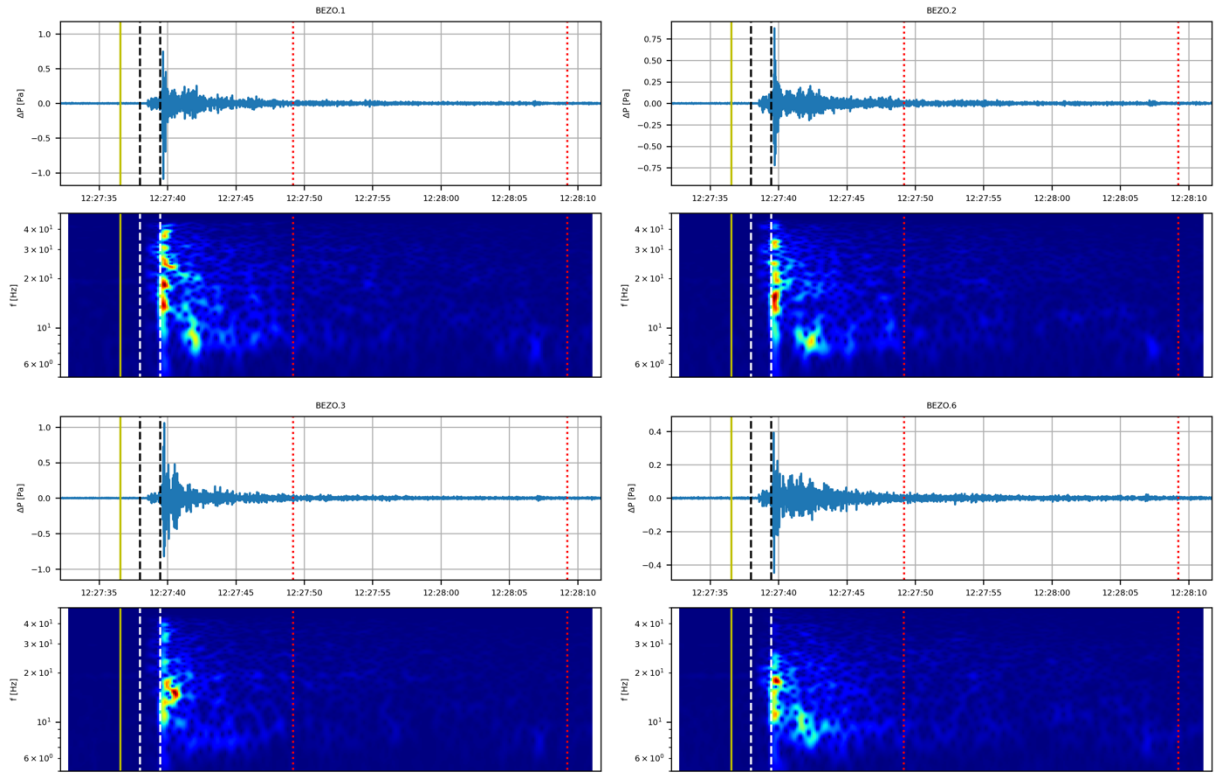

Figure 7. Waveforms and spectrograms of 5–50 Hz bandpassed recordings at BEZO elements 1, 2, 3, and 6.

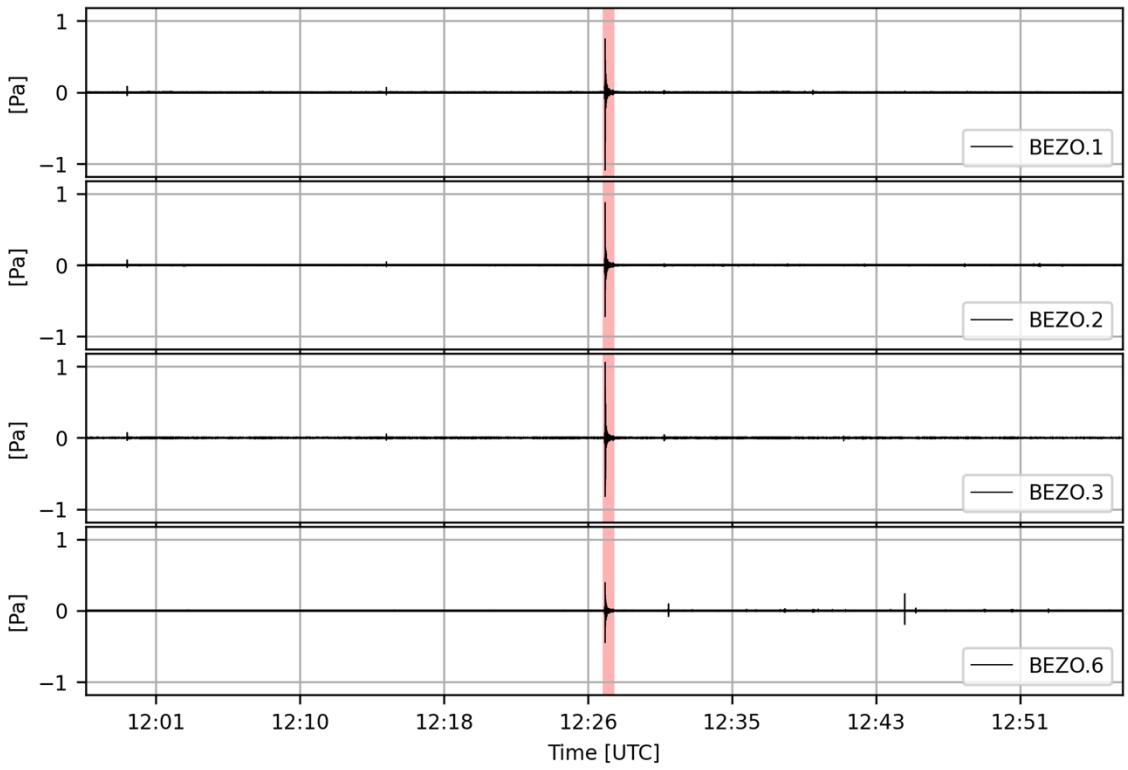

Figure 8. Waveforms highpassed above 5 Hz for BEZO elements 1, 2, 3, and 6. Waveforms show 30 minutes on either side of the earthquake origin time. The area highlighted in red is the time period shown in the previous figure.

5.1.2. Interpretation

The four signals observed at the BEZO array arrive at times of an expected seismic wave. Elements 1, 2, and 3 are not seismically decoupled; they record arrivals with amplitudes of 0.8–1.0 Pa. BEZO 6 is seismically decoupled and records an arrival with an amplitude is 0.4 Pa, approximately half. The seismic decoupling of the digital instruments cannot eliminate all effects of seismically-induced infrasound but is expected to significantly reduce the amplitude of such signals. We interpret these arrivals at BEZO as LIS, generated by seismic waves inducing vertical movement of the Earth's surface at the array.

5.2. Event tx2023bvwo

5.2.1. Results

An M2.9 earthquake with ID 'tx2023bvwo' occurred on January 27, 2023 at 04:47:14 UTC at a depth of 6.9±0.5 km. Infrasound signals were observed on BEZO 1, 2, 3, and 6; SHED 1, 2, 3, 5, and 6; and WIND 2 and 3. This earthquake occurred 38.3±0.4, 31.6±0.4, and 30.6±0.4 km from the central elements of the BEZO, SHED, and WIND arrays, respectively. As seen in Figure 9, each BEZO element records arrivals at two different times: one just after that of the predicted 3.5 km/s P-wave and the other with a celerity of approximately 0.535 km/s. Arrivals consist of 5–30 Hz waves with amplitudes of ~0.03–0.06 Pa. As seen in Figure 10, these arrivals are higher amplitude than the general noise conditions.

As seen in Figure 11, all five elements at SHED record two arrivals. The amplitudes of these arrivals are greater than the general noise conditions, as seen in Figure 12. The first arrival is shortly after the predicted arrival of the P-wave. The second occurs within the window expected for EIS with an amplitude of ~0.025 Pa. The celerity of this second arrival is approximately 0.345 km/s.

As seen in Figure 13, there is one arrival recorded at WIND 2 and 3. This arrival has an amplitude of ~0.025 Pa, which is of similar magnitude to the prevailing noise, as seen in Figure 14. The recording at WIND arrives in the expected EIS window with a celerity of about 0.335 km/s.

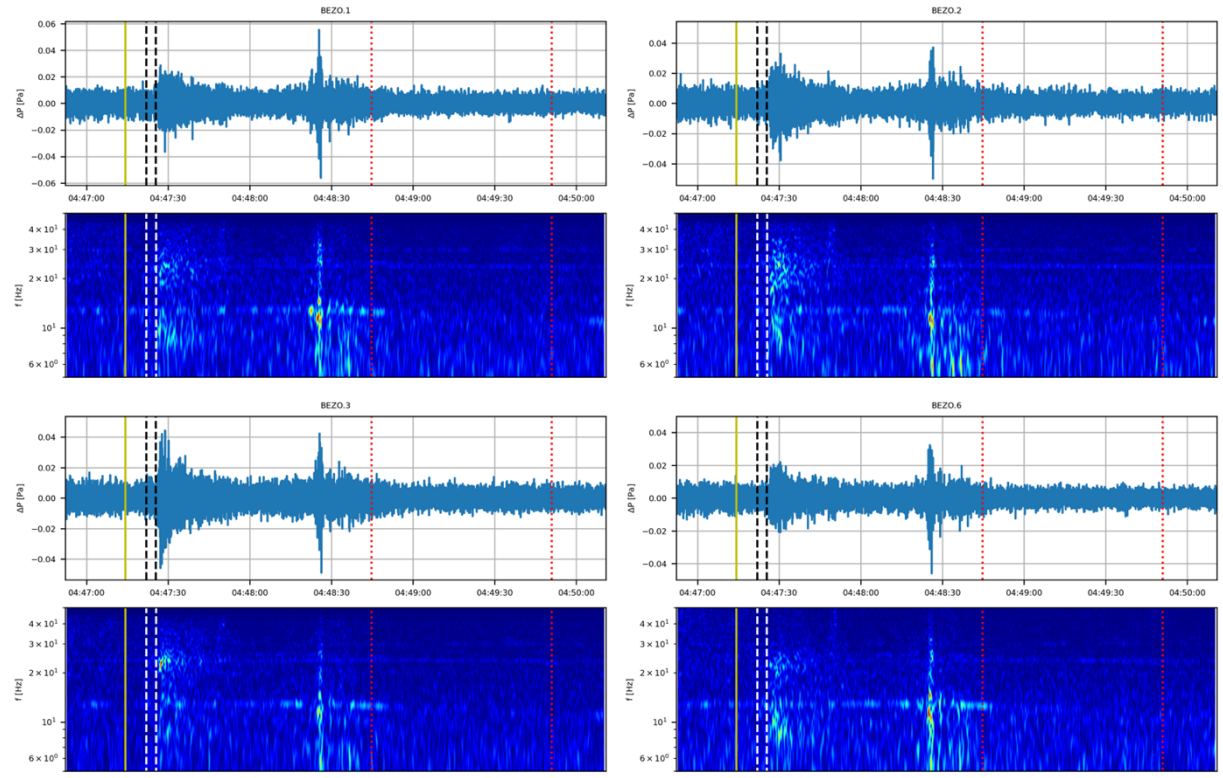

Figure 9. Waveforms and spectrograms of 5–50 Hz bandpassed infrasound recordings at BEZO elements 1, 2, 3, and 6.

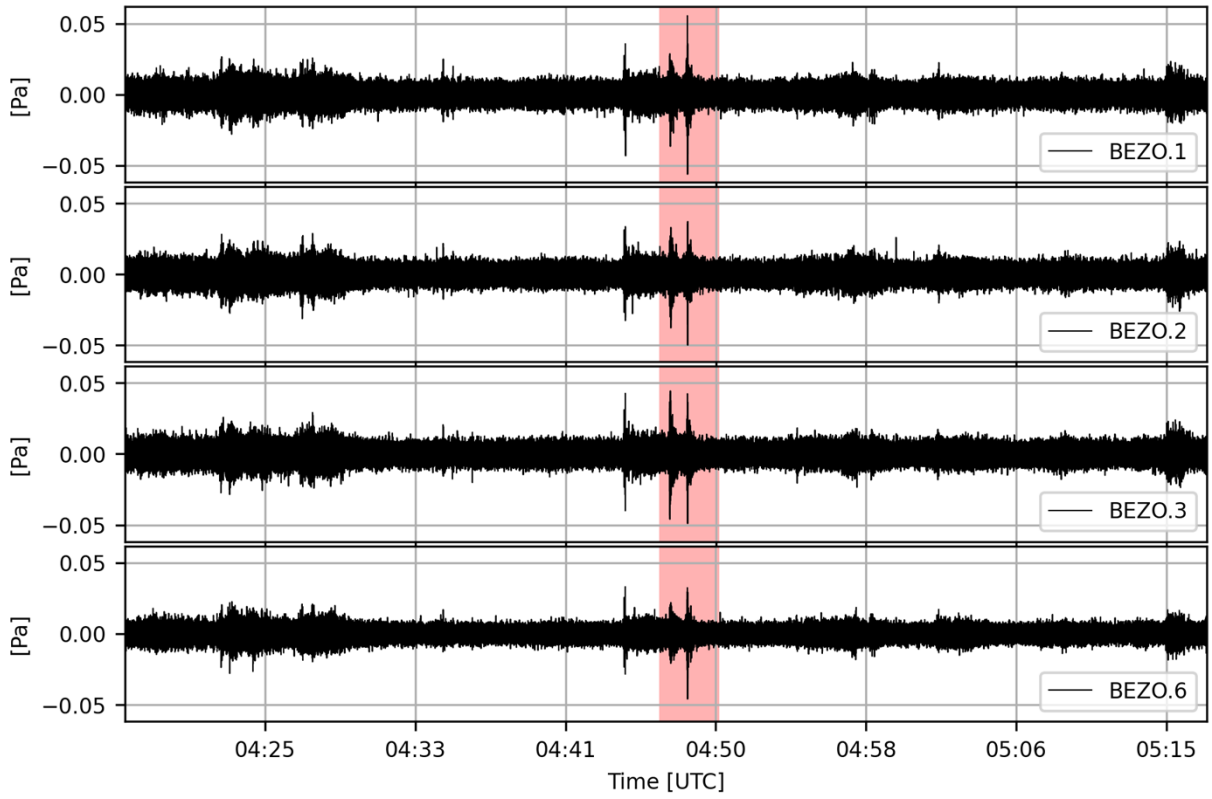

Figure 10. Waveforms highpassed above 5 Hz for BEZO elements 1, 2, 3, and 6. Waveforms show 30 minutes on either side of the earthquake origin time. The duration highlighted in red is the same as that shown in the previous figure.

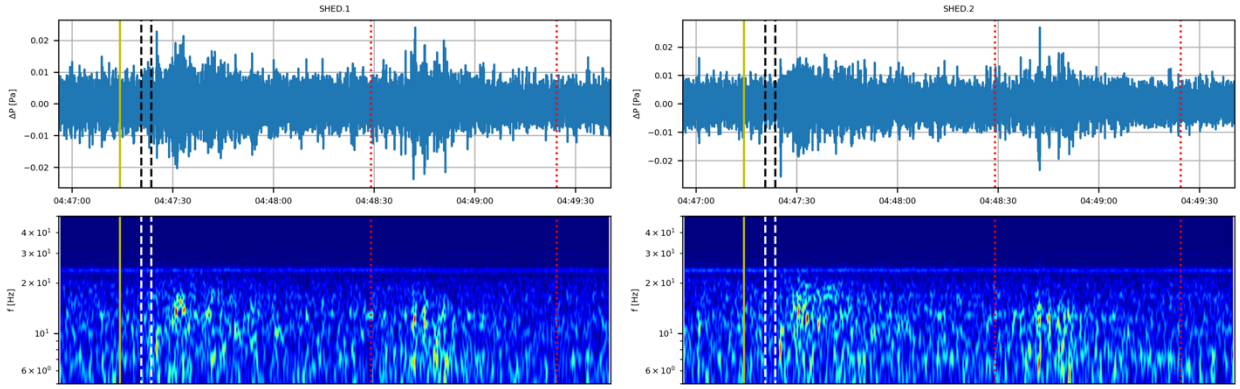

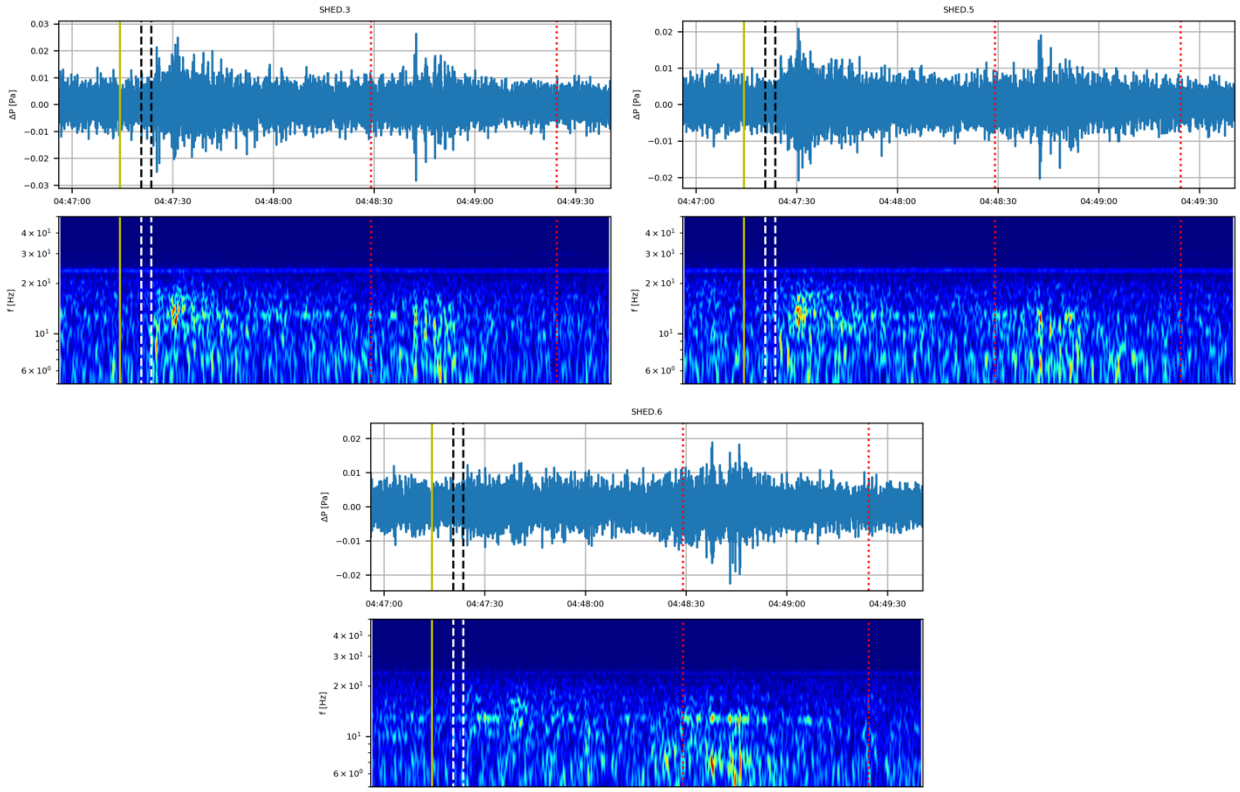

Figure 11. Waveforms and spectrograms of 5–20 Hz bandpassed infrasound recordings at SHED elements 1, 2, 3, 5, and 6. These were bandpassed for a narrower range to remove noise.

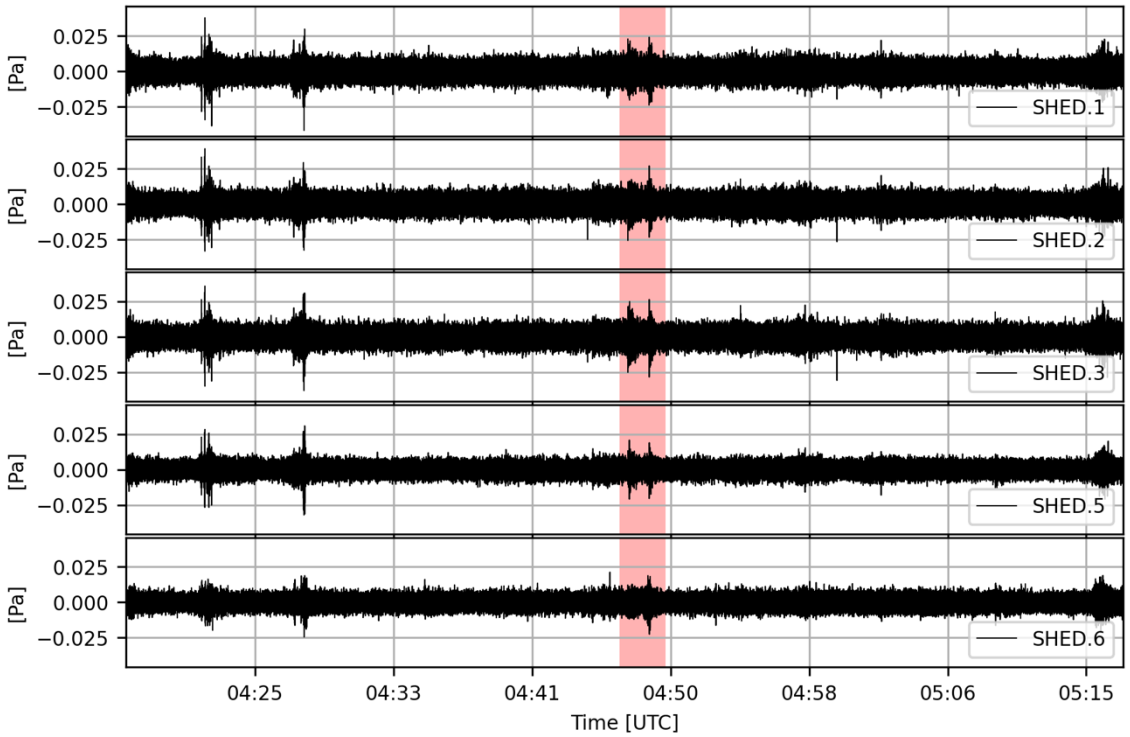

Figure 12. Waveforms bandpassed 5–20 Hz for SHED elements 1, 2, 3, 5, and 6. Waveforms show 30 minutes on either side of the earthquake origin time. The duration highlighted in red is the same as that shown in the previous figure.

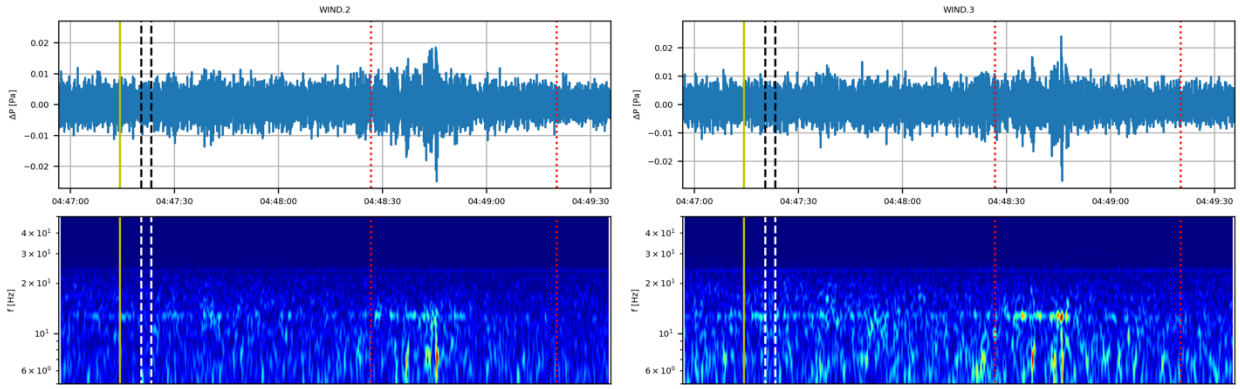

Figure 13. Waveforms and spectrograms of 5–20 Hz bandpassed infrasound recordings at WIND elements 2 and 3. These were bandpassed for a narrower range to remove noise.

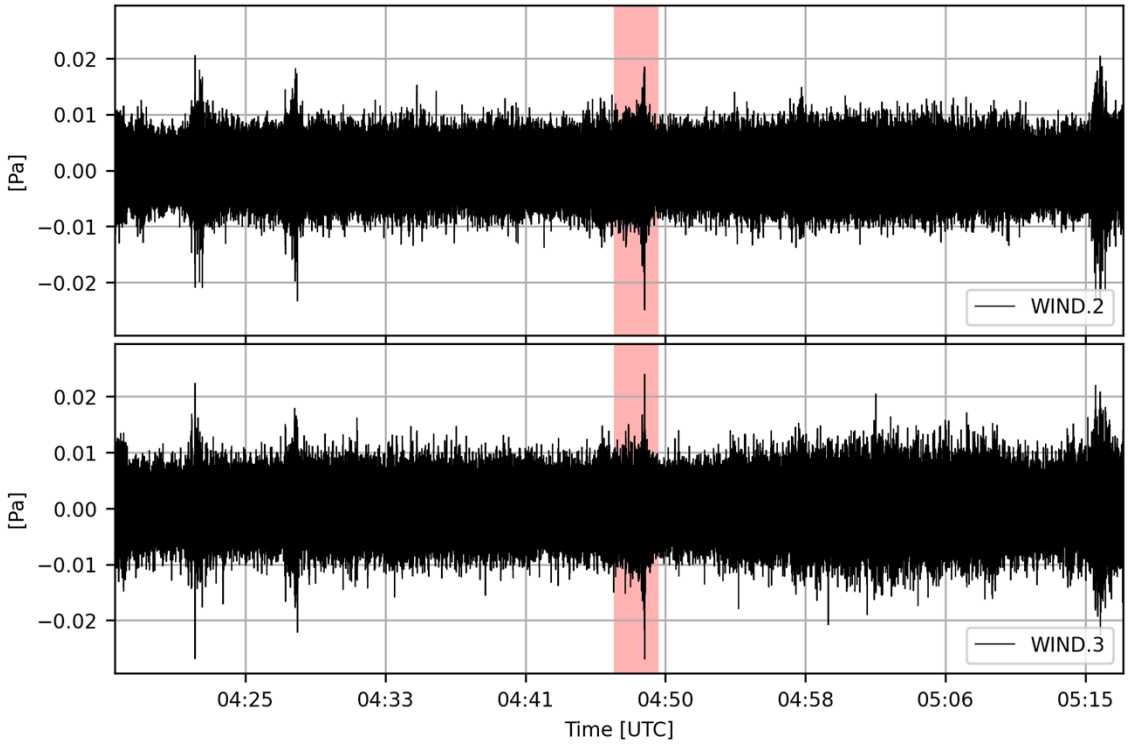

Figure 14. Waveforms bandpassed 5–20 Hz for WIND elements 2 and 3. Waveforms show 30 minutes on either side of the earthquake origin time. The duration highlighted in red is the same as that shown in the previous figure.

5.2.2. Interpretation

There are two apparent arrivals recorded at the BEZO and SHED arrays. The first arrival at each occurs around 04:47:30 UTC and is consistent with the predicted arrival of seismic waves. The first arrival has amplitudes of ~0.04 Pa at BEZO 1, 2, and 3 and ~0.02 Pa at BEZO 6. BEZO 6 is seismically decoupled while the other three are not. The first arrival at SHED has amplitudes of ~0.025 Pa. We take these observations together to interpret the first arrivals as LIS.

The second arrival has an amplitude of ~0.06 Pa at BEZO 1 and ~0.04 Pa at BEZO 2, 3, and 6. The amplitude at the BEZO 6, which is seismically decoupled, is like those recorded at the others, suggesting that the second arrival is not caused by seismically induced motion of the instrument and instead by a wave traveling through the atmosphere. It arrives, however, with a celerity of 0.535 km/s, which is too great for an acoustic velocity. The arrivals at both SHED and WIND, however, have celerities of 0.345 and 0.335 km/s, respectively, which are near the nominal value of the speed of sound.

Assuming that the second arrival is a from a single wavefront propagating across the network, it cannot have come directly from the earthquake. This feature arrives first at BEZO (04:48:25.5), the farthest away array, and last at WIND (04:48:46), the nearest array. The signal is not LIS or EIS generated by the earthquake.

5.3. Event tx2023cauk

5.3.1. Results

An M3.0 earthquake with ID 'tx2023cauk' occurred on January 29, 2023, at 21:22:27 UTC at a depth of 6.9±0.5 km. Coherent infrasound signals were observed on seven elements across two arrays: BEZO 2, 3, and 6 and SHED 2, 3, 5, and 6. Earthquake tx2023cauk occurred 10.0± 0.8 and 2.7± 0.8 km from the central elements of the BEZO and SHED arrays, respectively. As seen in Figure 15 and Figure 17, each infrasound observation is comprised of ~6–40 Hz waves with amplitudes of 0.08 – 0.8 Pa. All arrivals at BEZO occur just after the predicted arrival of a 3.5 km/s P-wave, as do three arrivals at SHED. There are also arrivals of ~10–30 Hz waves at SHED in the predicted window of EIS arrivals, with a celerity of approximately 0.380 km/s. As seen in Figure 16 and Figure 18, these observed IS signals are greater in amplitude than most noise conditions.

Array processing indicates that both arrivals at SHED elements 2, 3, and 5 propagate at a velocity >1 km/s (Figure 19). The back-azimuths of both arrivals appear to be ~-100°, though this value is less consistent for the second arrival. The true back azimuth to the earthquake is ~115°.

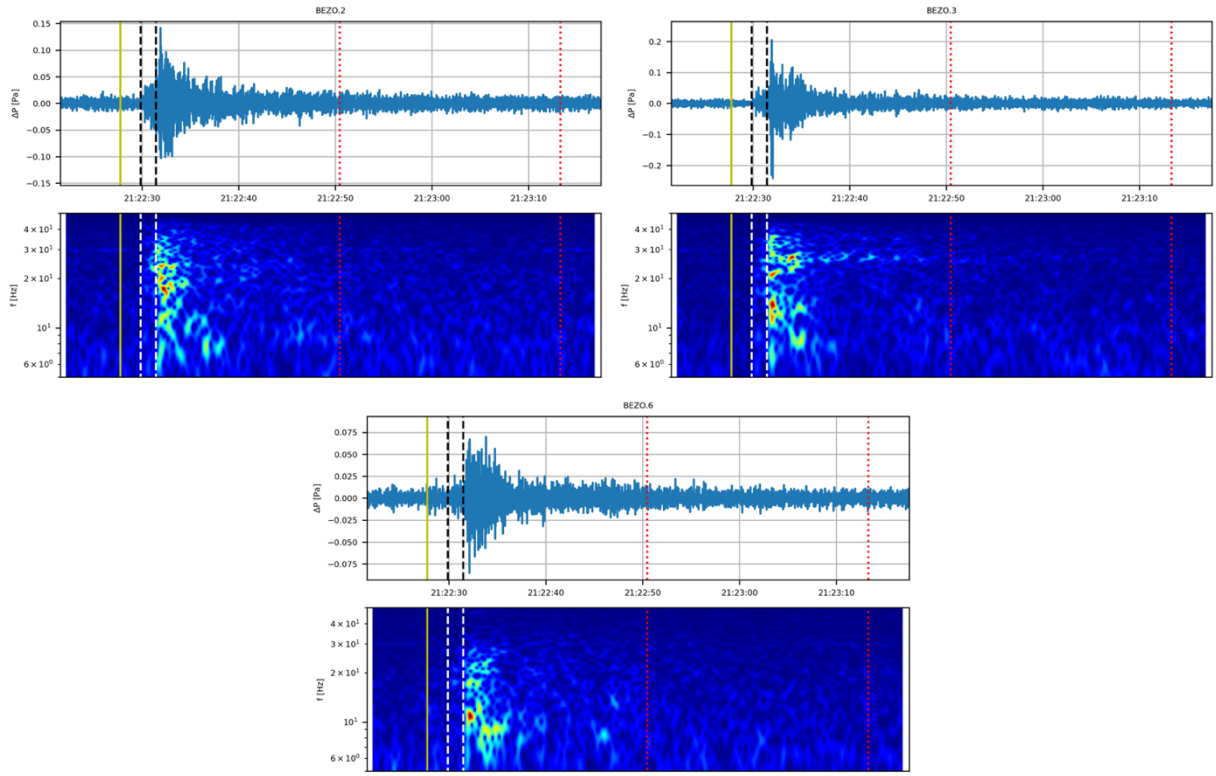

Figure 15. Waveforms and spectrograms of 5–50 Hz bandpassed infrasound recordings at BEZO elements 2, 3, and 6.

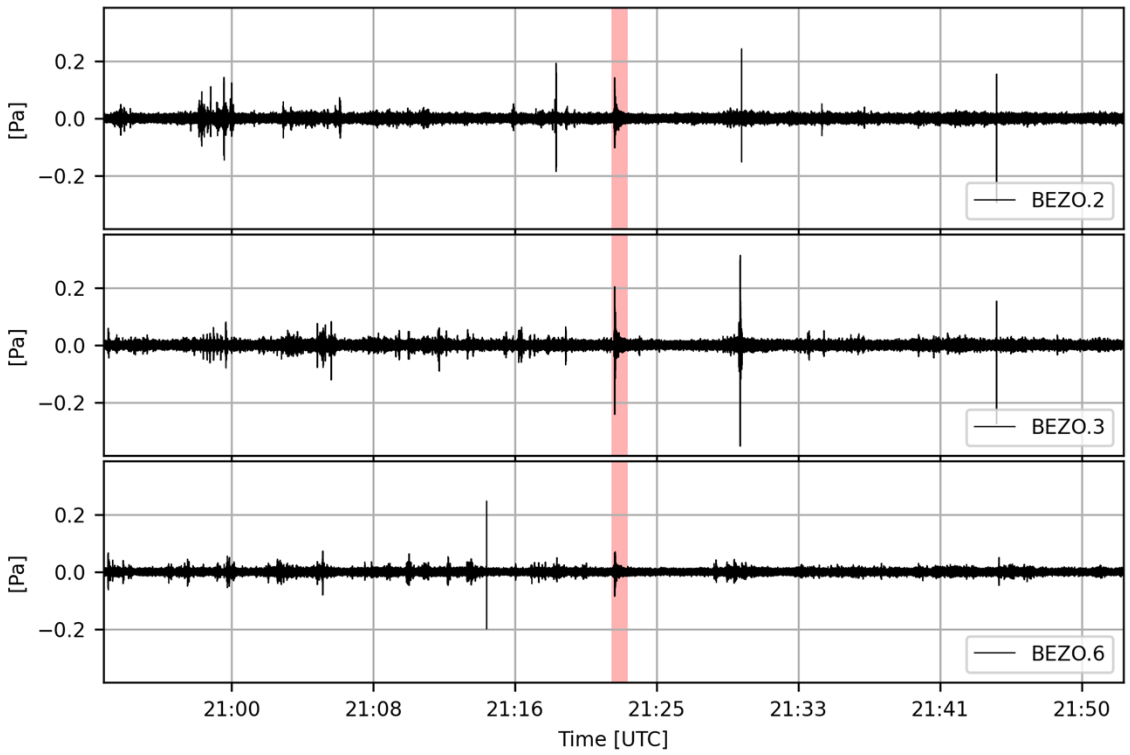

Figure 16. Waveforms highpassed above 5 Hz for BEZO elements 2, 3, and 6. Waveforms show 30 minutes on either side of the earthquake origin time. The duration highlighted in red is the same as that shown in the previous figure.

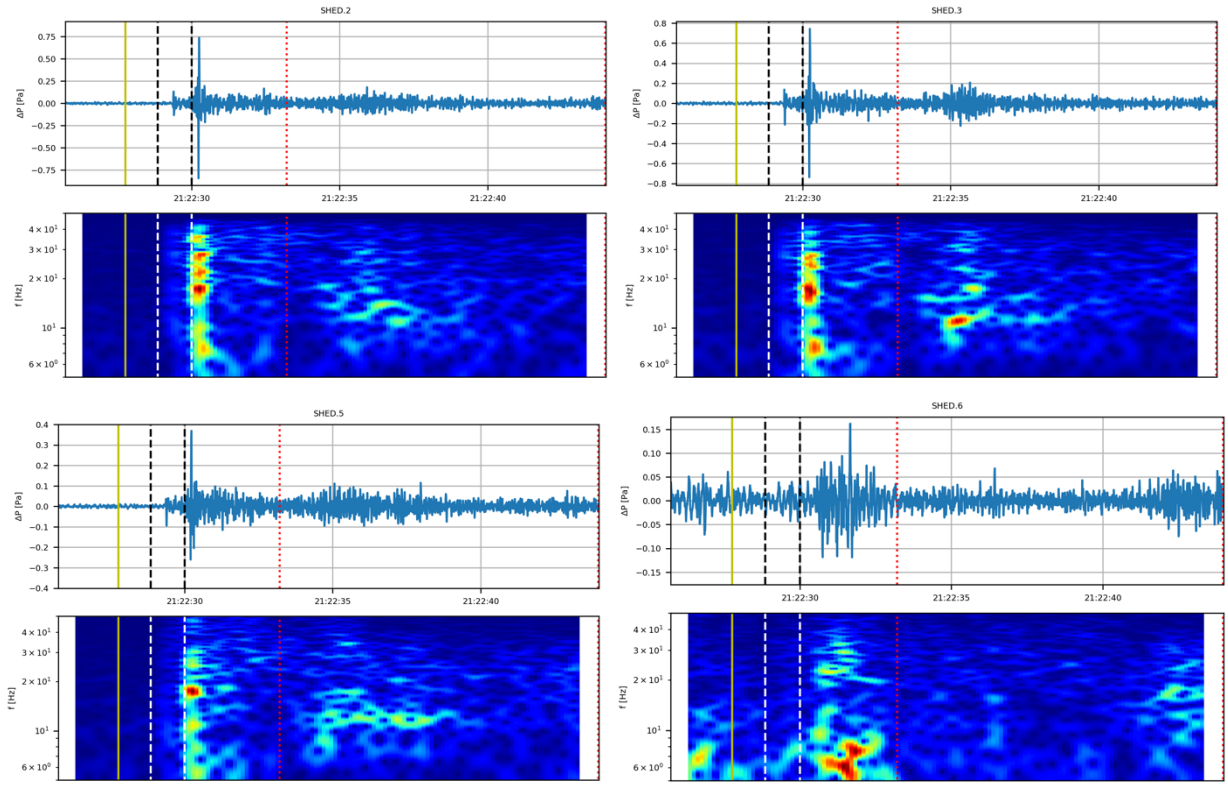

Figure 17. Waveforms and spectrograms of 5–50 Hz bandpassed infrasound recordings at SHED elements 2, 3, 5, and 6.

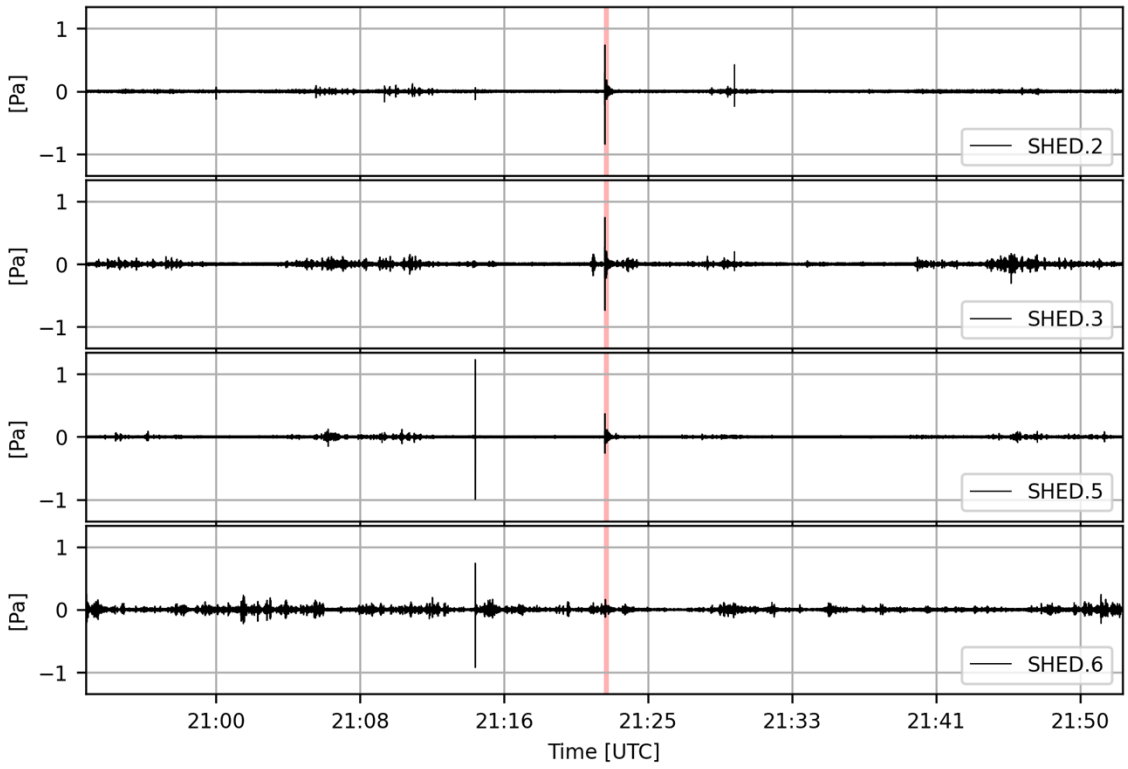

Figure 18. Waveforms highpassed above 5 Hz for SHED elements 2, 3, 5, and 6. Waveforms show 30 minutes on either side of the earthquake origin time. The duration highlighted in red is the same as that shown in the previous figure.

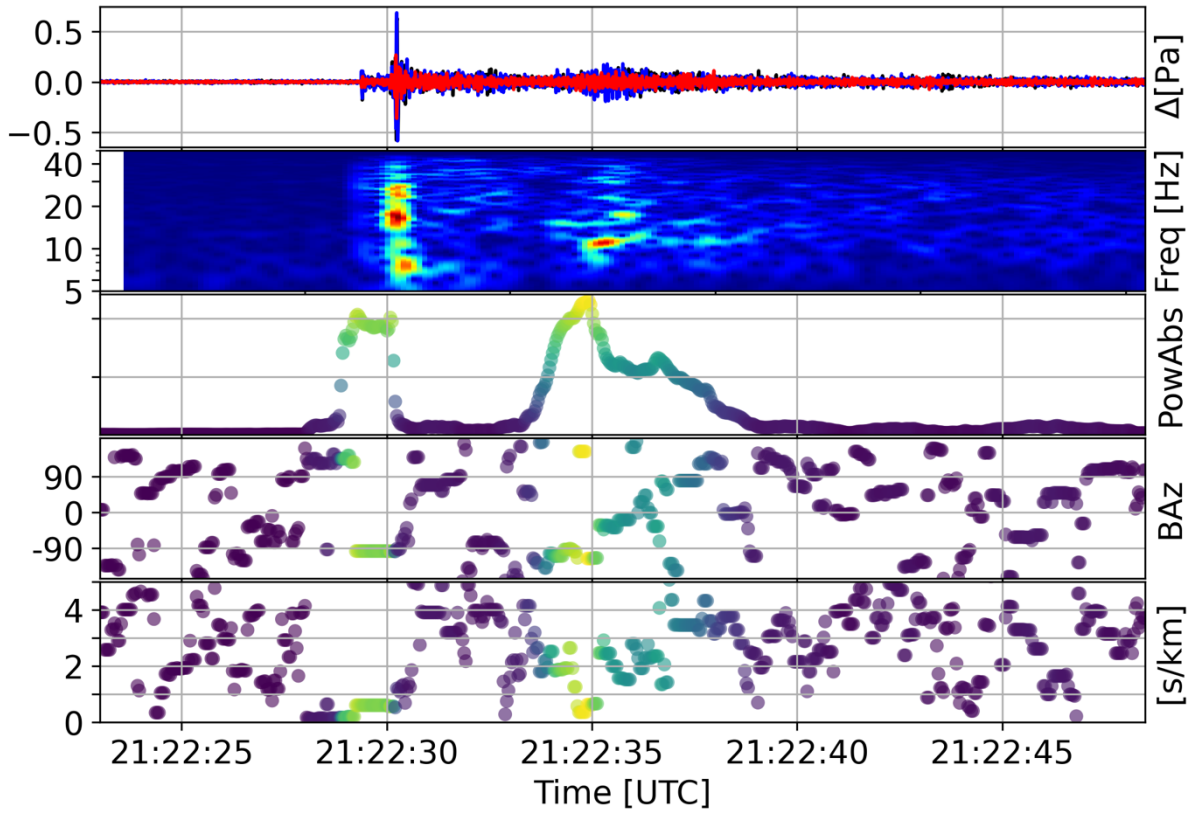

Figure 19. Array processing results for SHED elements 2, 3, and 5. The top panel shows the three waveforms plotted on top of one another. The spectrogram is for SHED 3. The third panel shows absolute power, the fourth back-azimuth in degrees and the bottom panel shows slowness of the propagating wavefront, the inverse of velocity. The color in the bottom three panes corresponds to the value of absolute power in the middle pane.

5.3.2. Interpretation

BEZO records a single arrival and SHED records two. The arrival at BEZO and the first one at SHED are consistent with the predicted arrival of seismic waves and are therefore interpreted here as LIS.

The second arrival at SHED occurs at a time consistent with the arrival of EIS with a celerity of ~0.38 km/s. Array analysis, however, indicates that this 10–12 Hz feature crosses the array at ~1 km/s or greater. If this result of the array analysis is true, then this feature cannot be associated with the earthquake. It could not be EIS or SIS, both of which would propagate across the array at an acoustic velocity. The arrival could also not be LIS because it would have arrived earlier. Further analysis of this arrival is warranted.

5.4. Event tx2023cayr

5.4.1. Results

An M2.9 earthquake with ID 'tx2023cayr' occurred on January 29, 2023, at 23:31:49 UTC at a depth of 4.5±0.8 km. Coherent infrasound signals were observed on eight instruments across all three arrays: BEZO 2, 3 and 6; SHED 2, 3, 5, and 6; and WIND 3. Earthquake tx2023cayr occurred 10.1± 1.0, 2.8± 1.0, and 4.4 ± 1.0 km from the central elements of the BEZO, SHED, and WIND arrays, respectively. As seen in Figures Figure 20Figure 22, Figure 24, each arrival is comprised of ~5–40 Hz waves with amplitudes of 0.15–0.6 Pa. All arrivals at BEZO occur just after the predicted arrival of a 3.5 km/s P-wave, as do some arrivals at SHED and WIND. Elements at SHED and WIND also capture a possible second arrival within the expected EIS window, with celerities of approximately 0.390 and 0.340 km/s, respectively. These arrivals are comprised of ~8–15 Hz waves. The amplitudes of the signals at BEZO and SHED are greater than that of the prevailing noise (Figures Figure 21Figure 23). The amplitudes of the recordings at WIND are less than that of the ambient noise (Figure 25).

Array processing of the two arrivals at SHED elements 2, 3, and 5 indicate that the first arrival propagates at a velocity of >1 s/km (Figure 26). The 10–12 Hz portion of the second arrival at SHED has a slowness of 2.5–3 s/km, corresponding to a trace velocity of 0.333–0.4 km/s. The back-azimuth suggests that the wave arrived from ~100–110°. The true back-azimuth between SHED and this event is 115°.

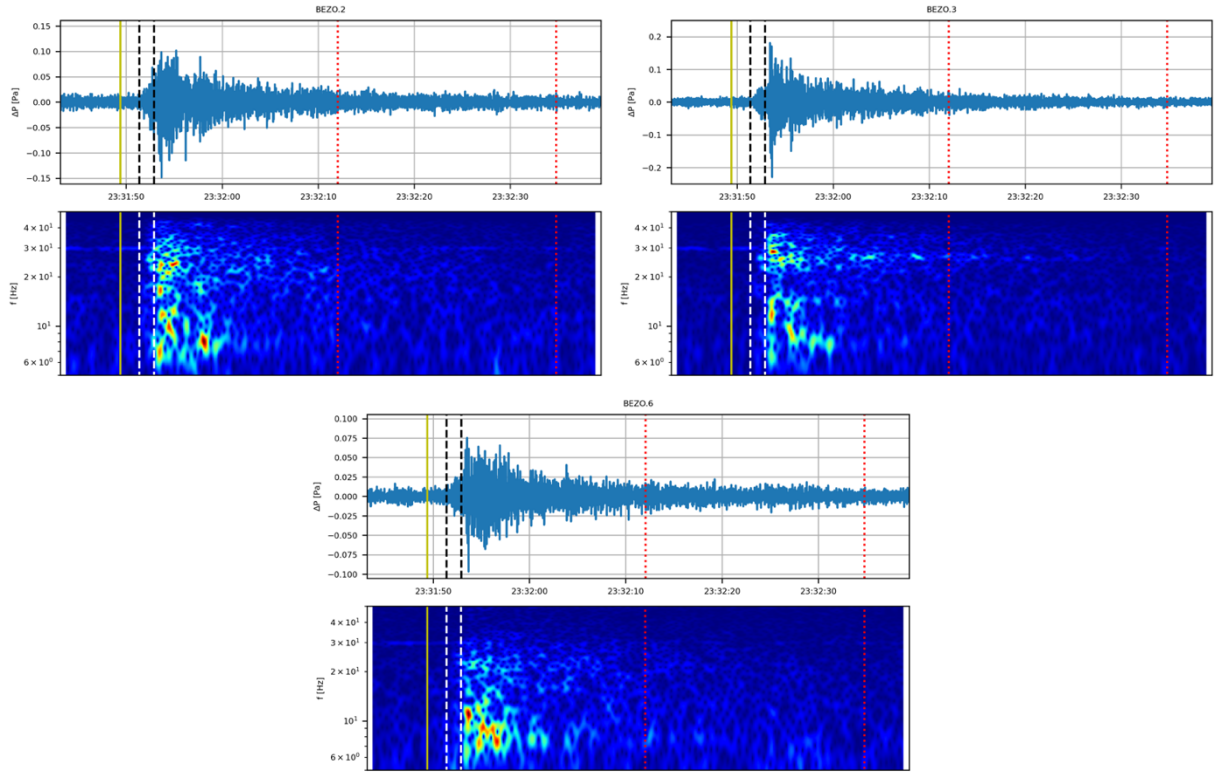

Figure 20. Waveforms and spectrograms of 5–50 Hz bandpassed infrasound recordings at BEZO elements 2, 3, and 6.

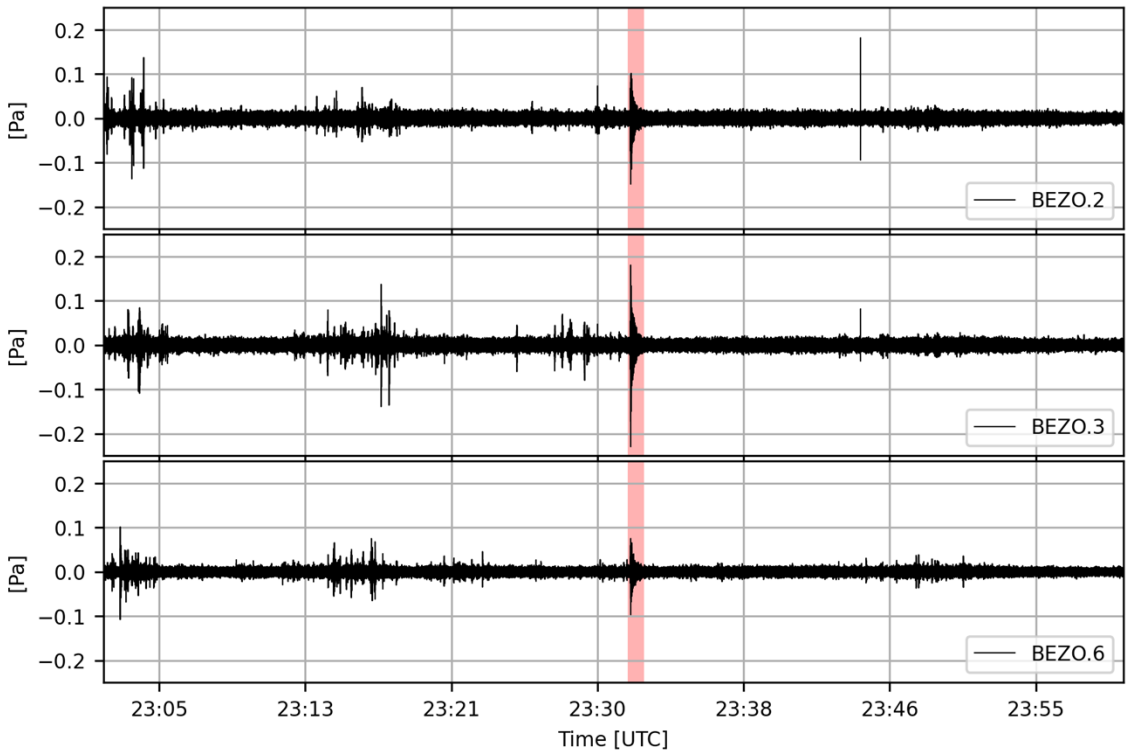

Figure 21. Waveforms highpassed above 5 Hz for BEZO elements 2, 3, and 6. Waveforms show approximately 30 minutes on either side of the earthquake origin time. The duration highlighted in red is the same as that shown in the previous figure.

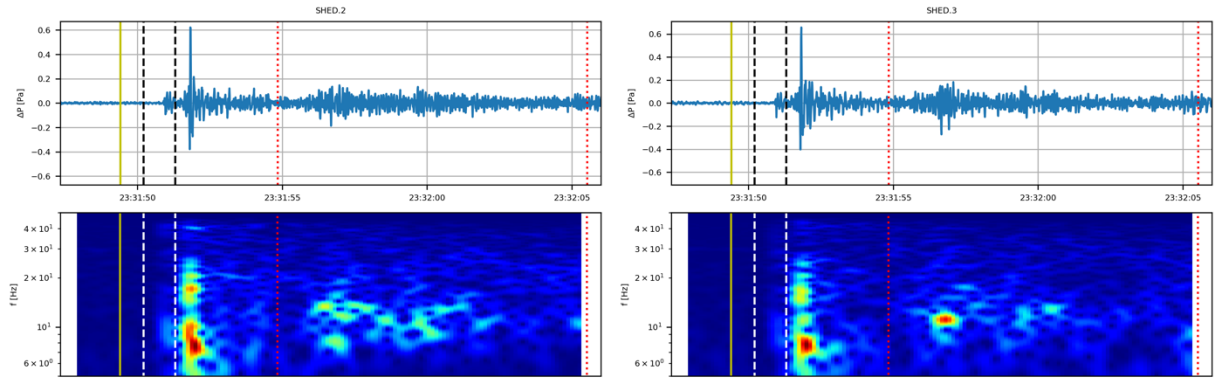

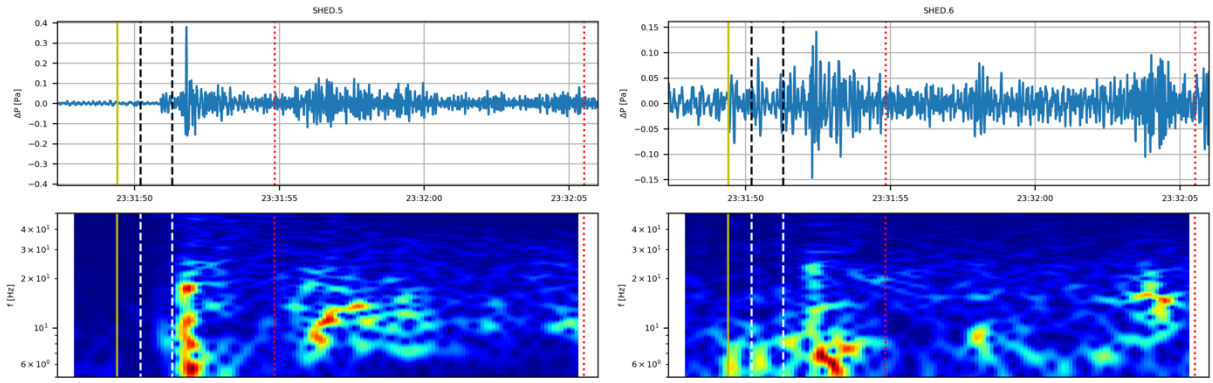

Figure 22. Waveforms and spectrograms of 5–50 Hz bandpassed infrasound recordings at SHED elements 2, 3, 5, and 6.

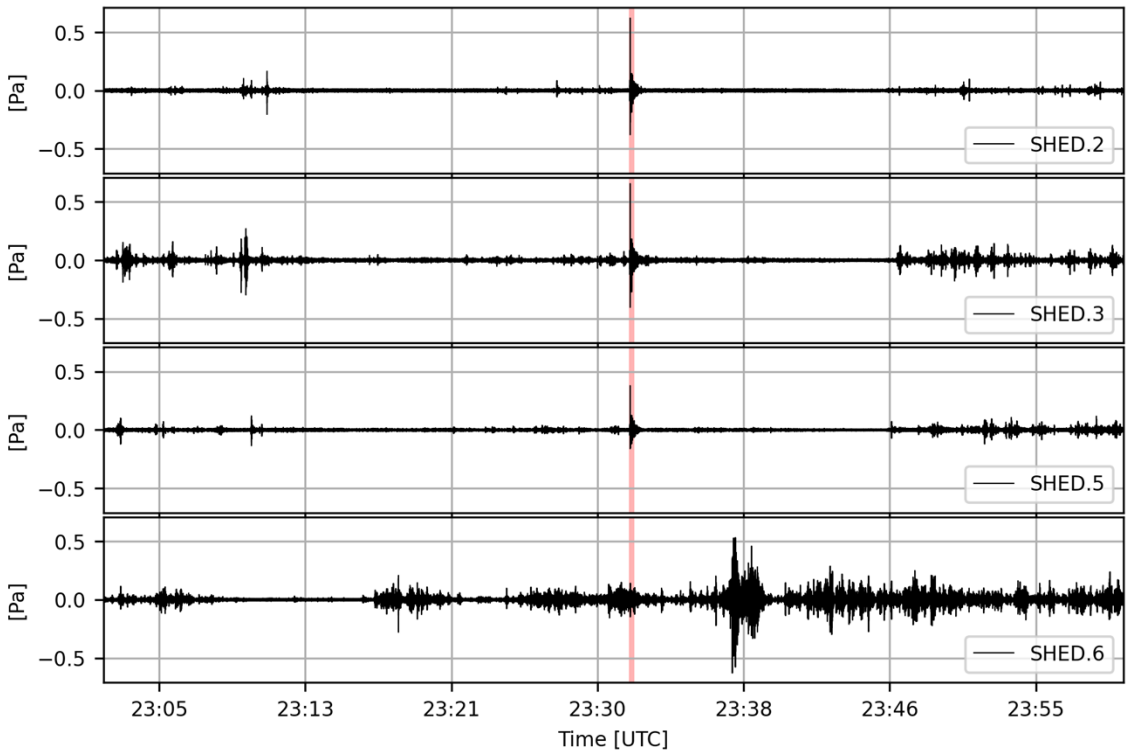

Figure 23. Waveforms highpassed above 5 Hz for SHED elements 2, 3, 5, and 6. Waveforms show approximately 30 minutes on either side of the earthquake origin time. The duration highlighted in red is the same as that shown in the previous figure.

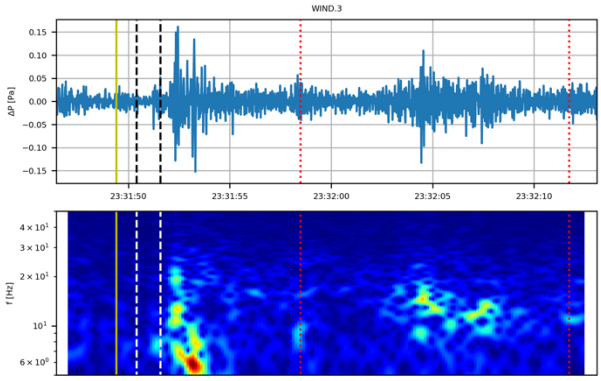

Figure 24. Waveforms and spectrograms of 5–50 Hz bandpassed infrasound recording at WIND element 3.

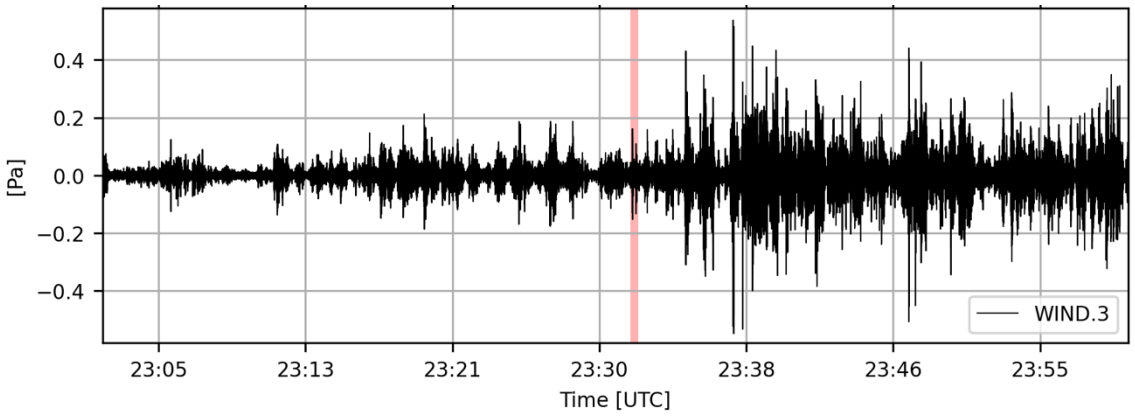

Figure 25. Waveform highpassed above 5 Hz for WIND element 3. Waveform shows approximately 30 minutes on either side of the earthquake origin time. The duration highlighted in red is the same as that shown in the previous figure.

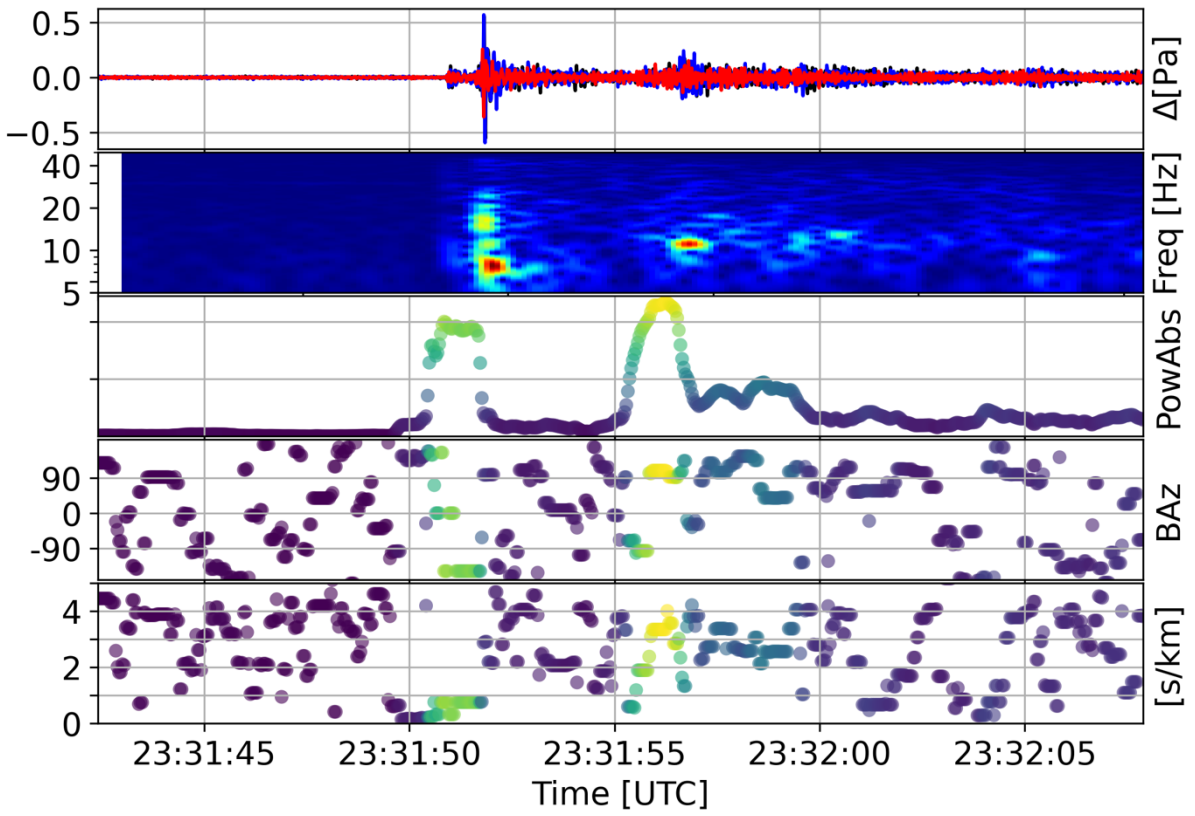

Figure 26. Array processing results for SHED elements 2, 3, and 5. The top panel shows the three waveforms plotted on top of one another. The spectrogram is for SHED 3. The third panel shows absolute power. The fourth panel shows back-azimuth in degrees. The bottom panel shows slowness of the propagating wavefront, the inverse of velocity. The color in the bottom three panes corresponds to the value of absolute power in the middle pane.

5.4.2. Interpretation

There is one arrival at BEZO, occurring at a time consistent with the arrival of seismic waves. The amplitudes of the recording at BEZO 6, which is seismically decoupled, is about one-half to two-thirds of that recorded at the others. These observations support the interpretation of this arrival as LIS.

There are two arrivals recorded on SHED 2, 3 and 5. (SHED 6 appears to be an outlier and isn't included here). The first one occurs at a time consistent with the arrival of seismic waves. The amplitude on SHED 5, the seismically decoupled instrument, is about two-thirds of that recorded on the others. Array processing also indicates propagation velocities of this wave across the array as >1 km/s. These observations support the interpretation that this signal is an arrival of LIS.

The second arrival at SHED has a celerity of 0.380 km/s. The array processing likewise indicates a range of velocities of the wavefront (0.250–0.400 km/s) that are consistent with acoustic propagation. The array processing also calculates back-azimuth of ~110°, which is consistent with the known value of 115°. The amplitude of the arrival at SHED 5, which is seismically decoupled, is about 0.1 Pa, about half the value of the others. This implies that this arrival may be LIS, generated

by arriving seismic waves. The bulk of the evidence, however, is consistent with this being EIS. Further analysis to confirm this signal as EIS is warranted.

5.5. Event tx2023cbwa

5.5.1. Results

An M2.5 earthquake with ID 'tx2023cbwa' occurred on January 30, 2023 at 11:19:58 UTC at a depth of 7.5±0.9 km. Coherent infrasound signals were observed on BEZO elements 2, 3, and 6, SHED elements 2, 3, 5, and 6, and WIND elements 2 and 3. This earthquake occurred 21.5±0.7 and 14.1±0.7, and 14.6±0.7 km from the central elements of the BEZO, SHED, and WIND arrays, respectively. As seen in Figures Figure 27, Figure 29, Figure 31, each infrasound observation is comprised of ~15–40 Hz waves with amplitudes of 0.02–0.08 Pa. Several arrivals occur just after the predicted arrival of a 3.5 km/s P-wave. Arrivals at BEZO occur near the earliest predicted arrival of an EIS wave traveling at 0.425 km/s. Arrivals at SHED occur in the middle of the predicted EIS window, consistent with an EIS wave traveling at approximately 0.340 km/s. Figure 28 shows that the amplitudes of the signals at BEZO are greater than that of prevailing background noise. Figure Figure 30 and Figure 32 shows that the amplitudes of the signals recorded at SHED and WIND are comparable to that of noise.

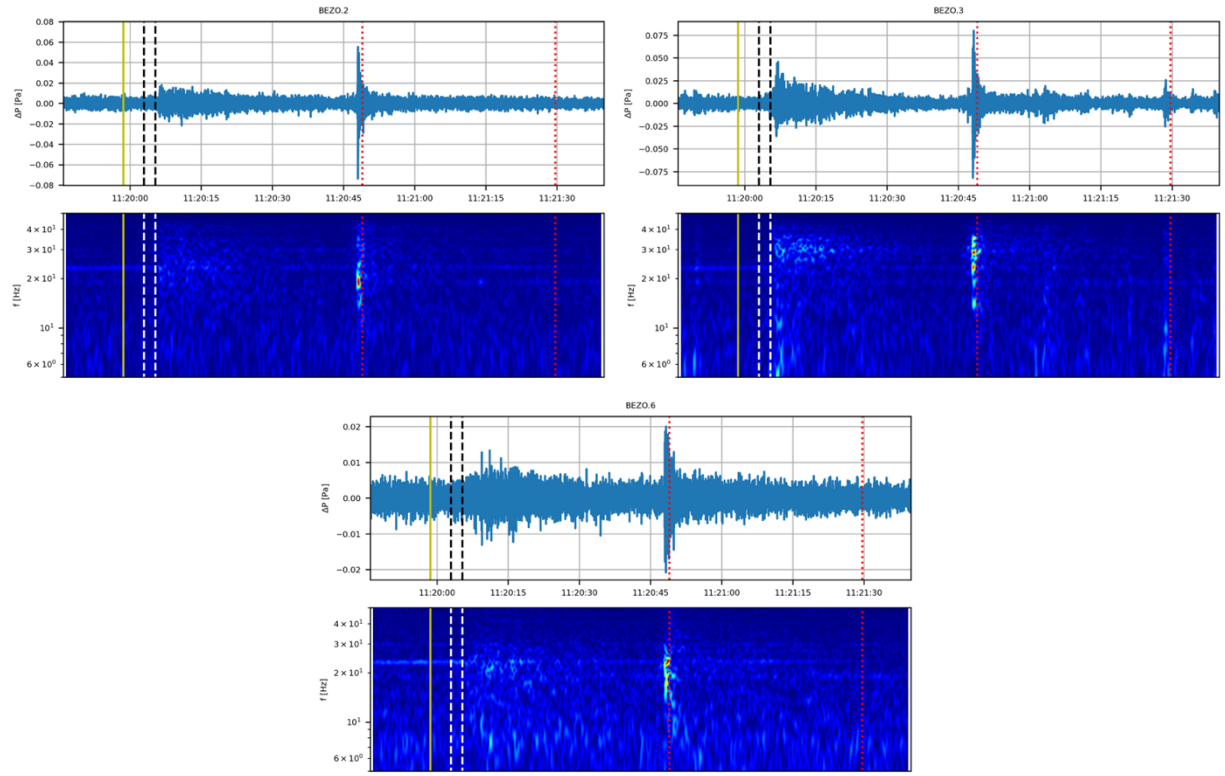

Figure 27. Waveforms and spectrograms of 5–50 Hz bandpassed infrasound recording at BEZO elements 2, 3, and 6.

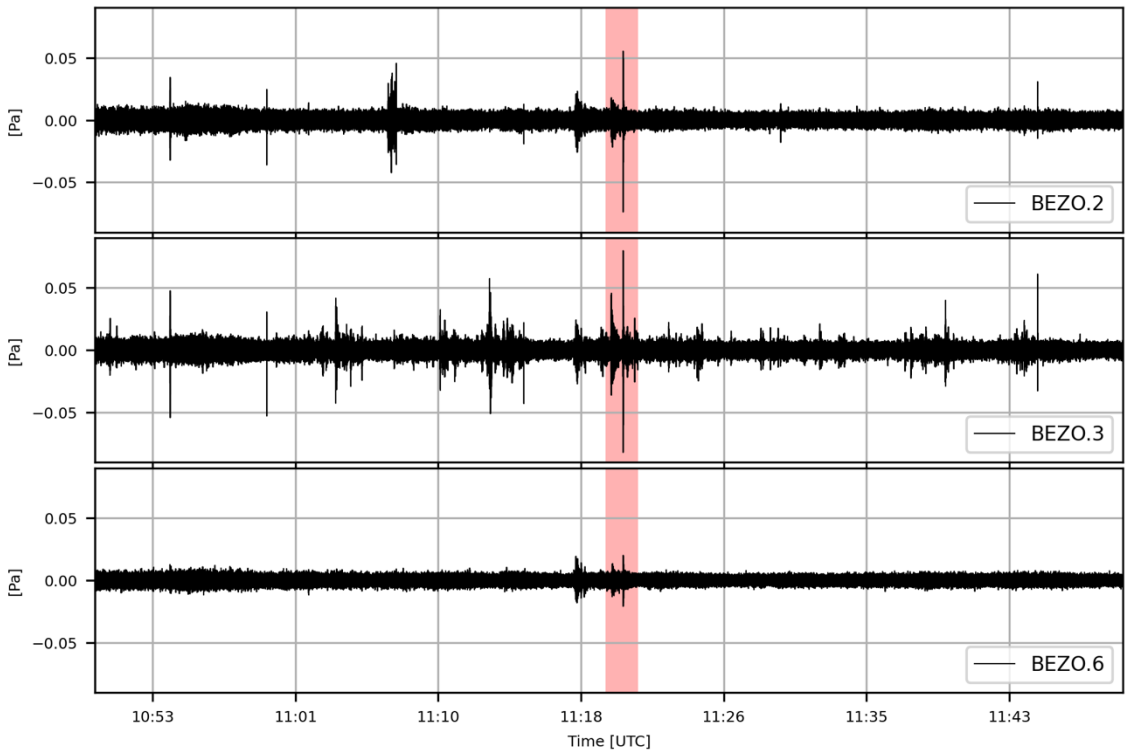

Figure 28. Waveforms highpassed above 5 Hz for BEZO elements 2, 3, and 6. Waveforms show 30 minutes on either side of the earthquake origin time. The duration highlighted in red is the same as that shown in the previous figure.

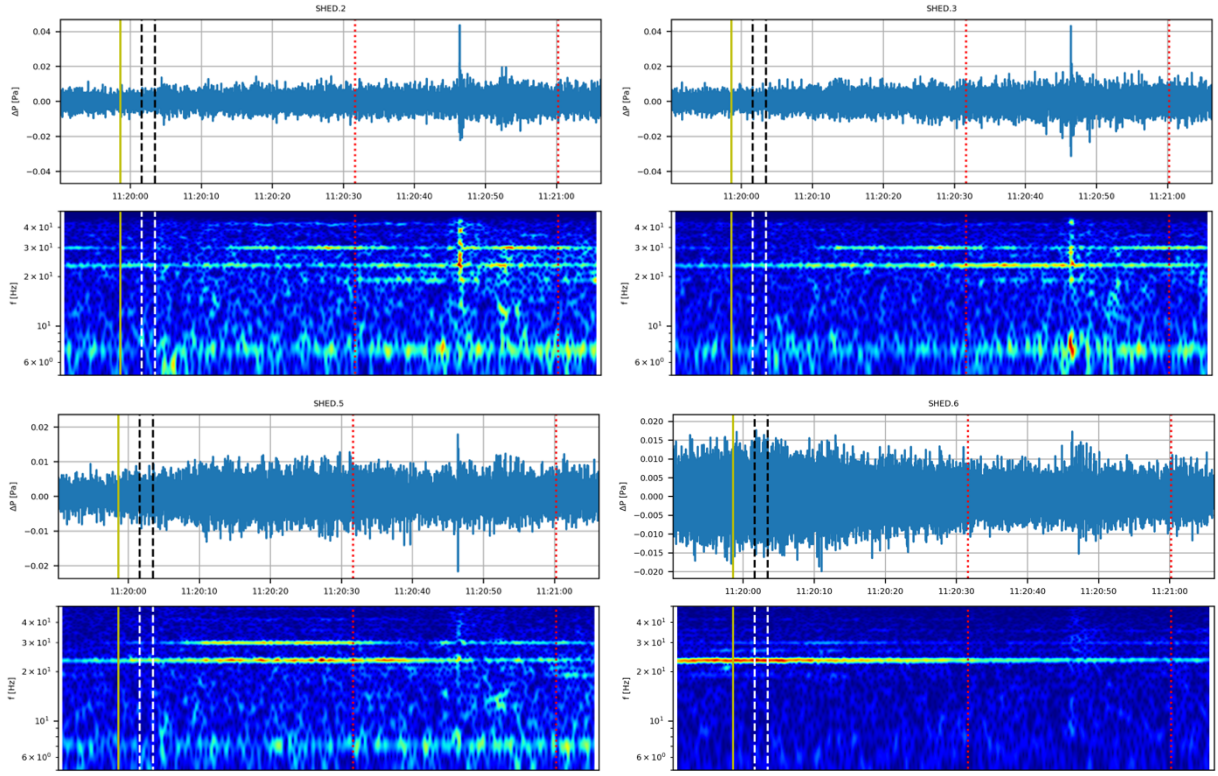

Figure 29. Waveforms and spectrograms of 5–50 Hz bandpassed infrasound recording at SHED elements 2, 3, 5, and 6.

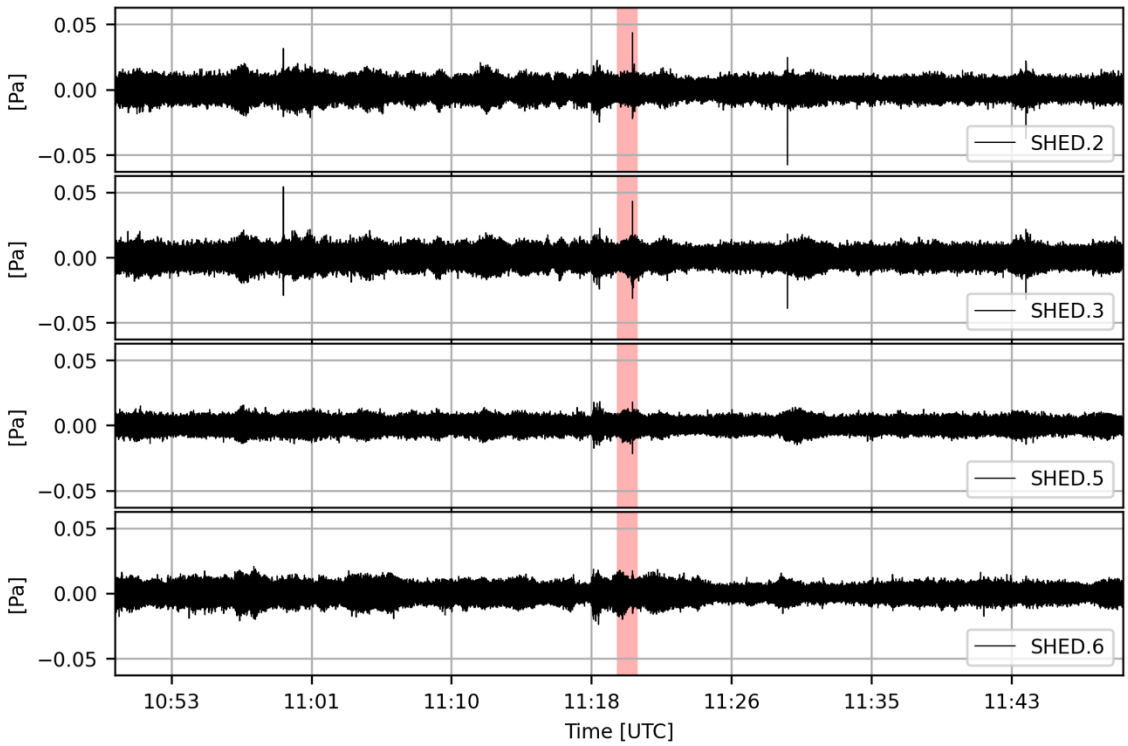

Figure 30. Waveforms highpassed above 5 Hz for SHED elements 2, 3, 5, and 6. Waveforms show 30 minutes on either side of the earthquake origin time. The duration highlighted in red is the same as that shown in the previous figure.

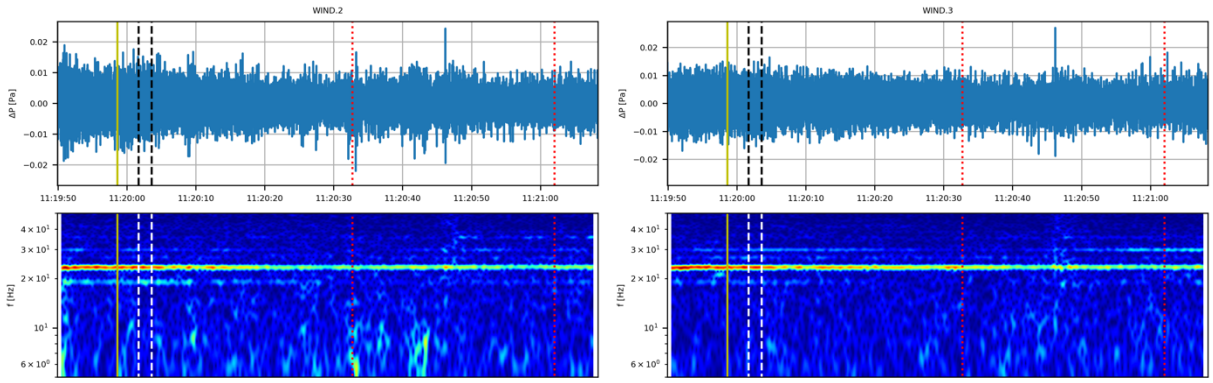

Figure 31. Waveforms and spectrograms of 5–50 Hz bandpassed infrasound recording at WIND elements 2 and 3.

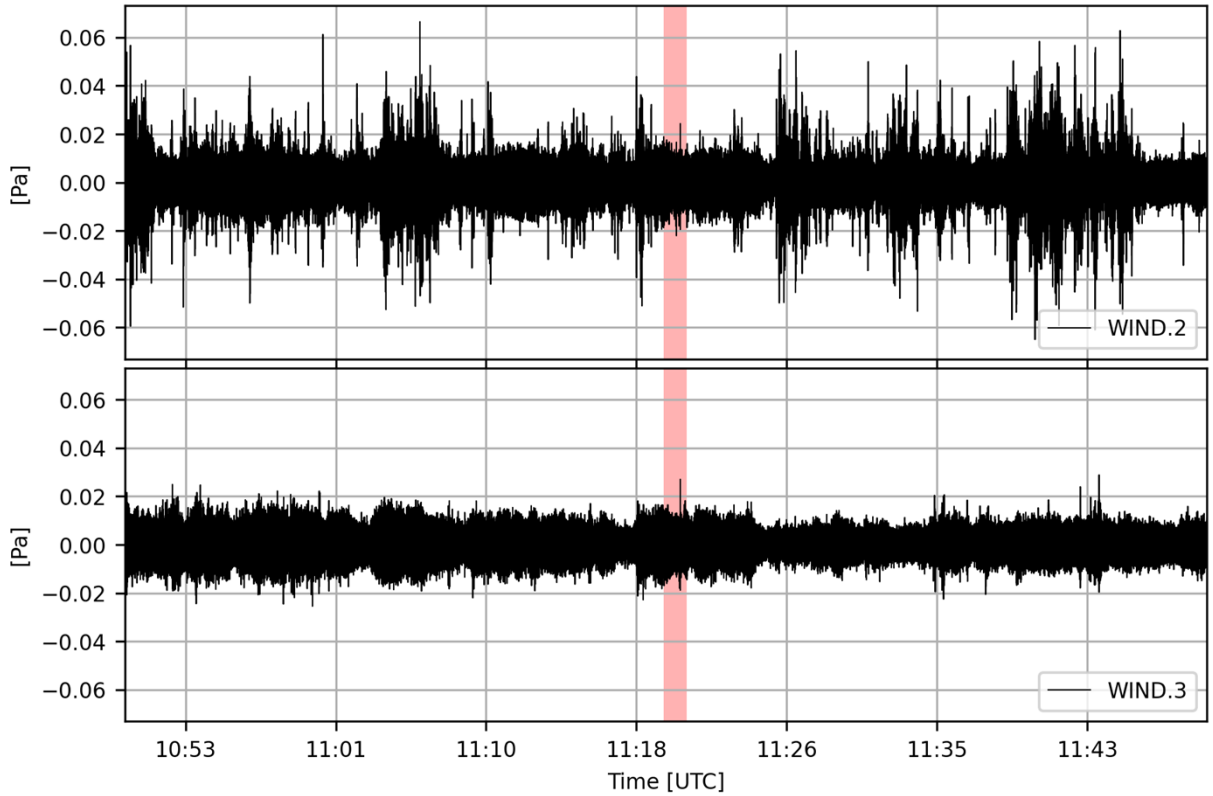

Figure 32. Waveforms highpassed above 5 Hz for WIND elements 2 and 3. Waveforms show 30 minutes on either side of the earthquake origin time. The duration highlighted in red is the same as that shown in the previous figure.

5.5.2. Interpretation

Arrivals are most obvious at the BEZO array and are much fainter at the other two. The celerities of the arrivals at SHED and WIND are 0.294 and 0.308 km/s, respectively, while the celerity of the arrival at BEZO is about 0.435 km/s. SHED and WIND are nearly equidistant from the epicenter, at 14.1 and 14.6 km, respectively, while BEZO is 21.5 km away.

While the arrivals at SHED and WIND have celerities that are consistent with EIS emanating from the epicenter, the celerity of the arrival at BEZO is too fast. The signal arrives first at WIND, next at SHED a half-second or so later, and lastly at BEZO another 1.5 seconds after that. Two seconds between the arrival at WIND to the arrival at BEZO is not enough time for an acoustic wave to travel the ~7.4 km separating them. Therefore, the signals observed at these three arrays cannot all be from a single EIS wavefront emanating from the epicenter.

It is possible that these signals are all related to and caused by the earthquake. The signals observed at SHED and WIND may be EIS emanating from the epicenter. The signal observed at BEZO may be SIS, caused by shaking of a nearby topographic feature. In this case, the EIS signal traveled ~14 km to SHED and WIND but did not make the additional 7 km to BEZO or was so low amplitude that it was not recorded as a signal. It is also possible that these signals were caused by something completely unrelated to the earthquake. There are many sources of infrasound noise, and it is possible that our window of interest happened to coincide with the arrival of infrasound generated by something else. An acoustic wave associated with a meteor, for instance, would arrive nearly vertically and could therefore arrive at all three arrays within two seconds and appear coherent. We find these arrivals inconclusive but err on the side of interpreting them as being unassociated with the earthquake.

5.6. Event tx2023cdzu

5.6.1. Results

An M2.5 earthquake with ID 'tx2023cdzu' occurred on January 31, 2023 at 15:30:03 UTC at a depth of 6.1±0.7 km. Infrasound signals were observed on BEZO elements 2, 3, and 6 and SHED elements 1, 2, 3, 5, and 6. The event occurred 8.5±1.0 km and 3.5±1.0 km from the central elements of the BEZO and SHED arrays, respectively. As seen in Figure 33, arrivals at BEZO consist of ~7–40 Hz waves with amplitudes of ~0.2–0.8 Pa. These arrivals have amplitudes greater than that of background noise, as seen in Figure 34. The recordings at SHED contain several features but the only consistent ones are at elements 2, 3, and 5. As seen in Figure 35, arrivals at these elements consist of 6–40 Hz waves with amplitudes of 0.08–0.1 Pa. These amplitudes are like that of background noise, as seen in Figure 36. All arrivals occur around the predicted arrival window for a 3.5 km/s P-wave.

There is a possible second arrival of ~10–20 Hz energy at SHED elements 2, 3, and 5. The amplitude of this feature is not consistent across the three instruments, ranging from 0.025 to 0.045 Pa. This feature occurs in the early part of the EIS window.

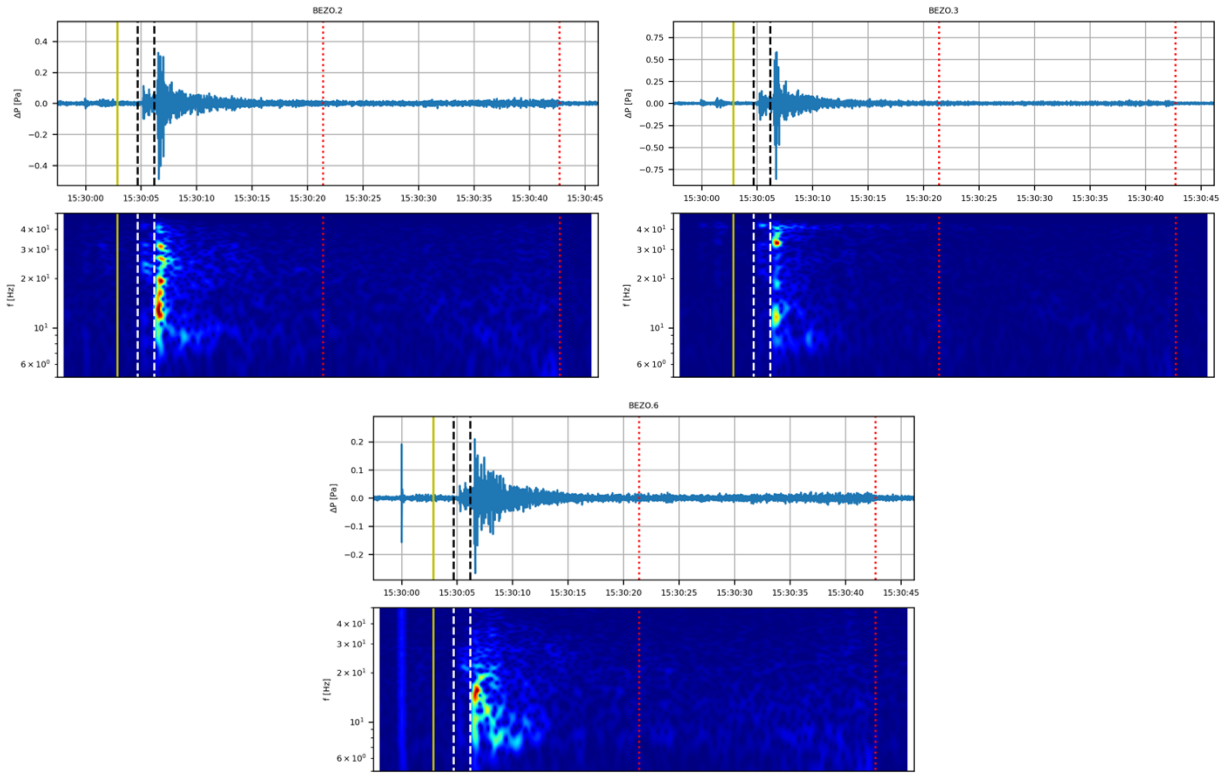

Figure 33. Waveforms and spectrograms of 5–50 Hz bandpassed infrasound recordings at BEZO elements 2, 3, and 6.

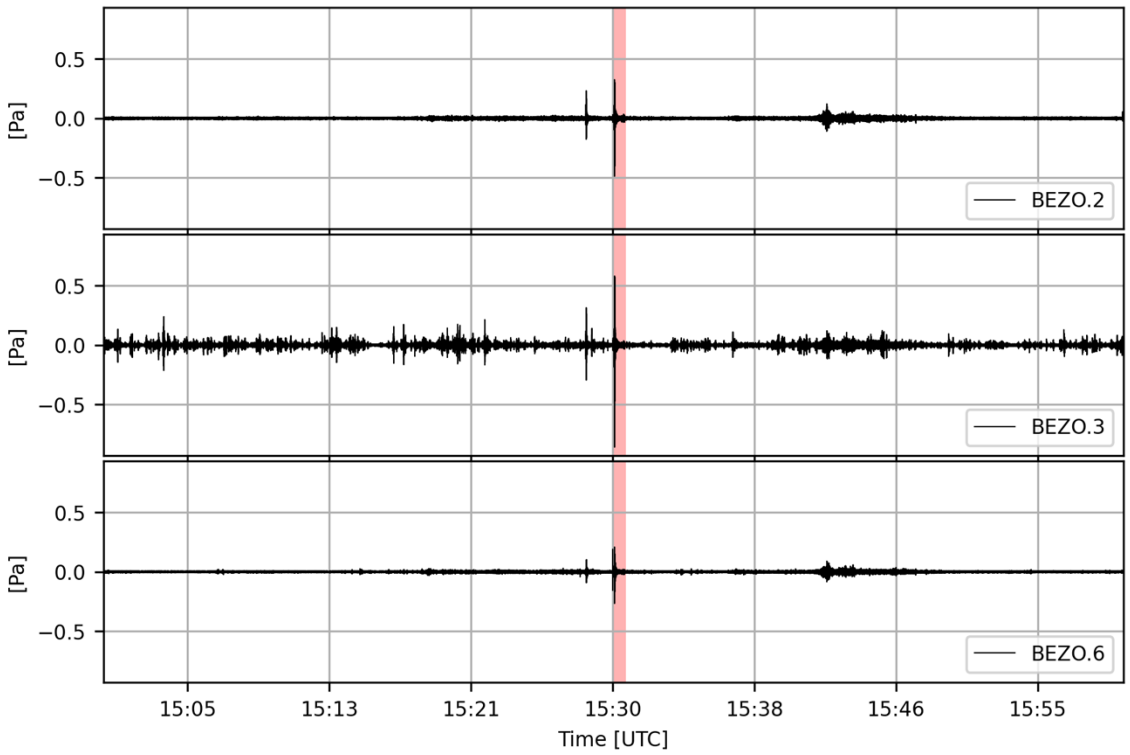

Figure 34. Waveforms highpassed above 5 Hz for BEZO elements 2, 3, and 6. Waveforms show 30 minutes on either side of the earthquake origin time. The duration highlighted in red is the same as that shown in the previous figure.

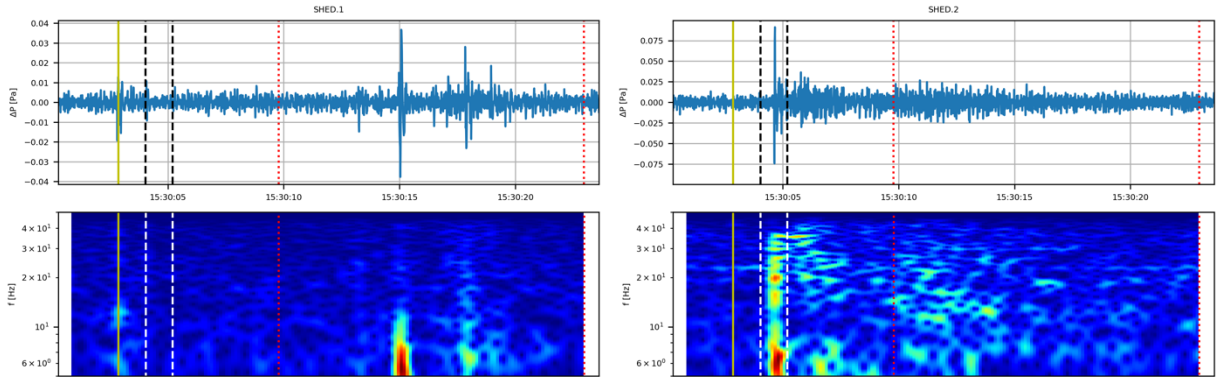

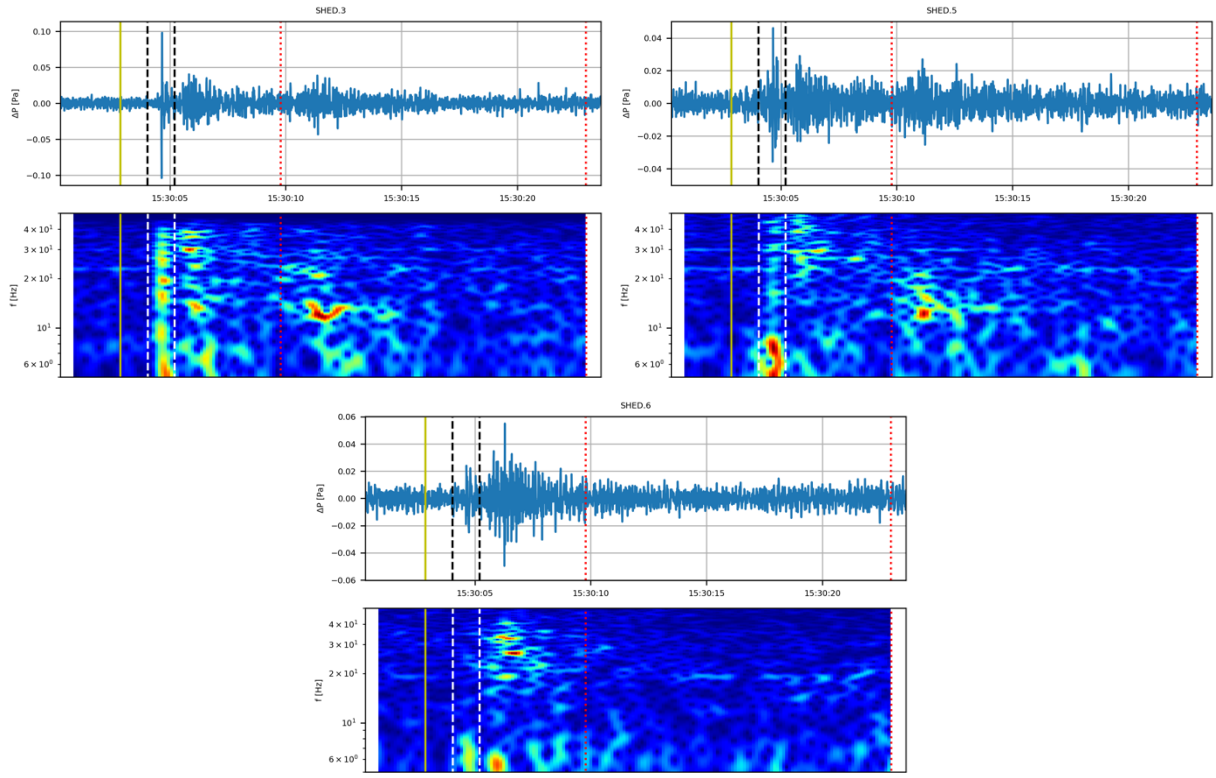

Figure 35. Waveforms and spectrograms of 5–50 Hz bandpassed infrasound recordings at SHED elements 1, 2, 3, 5, and 6.

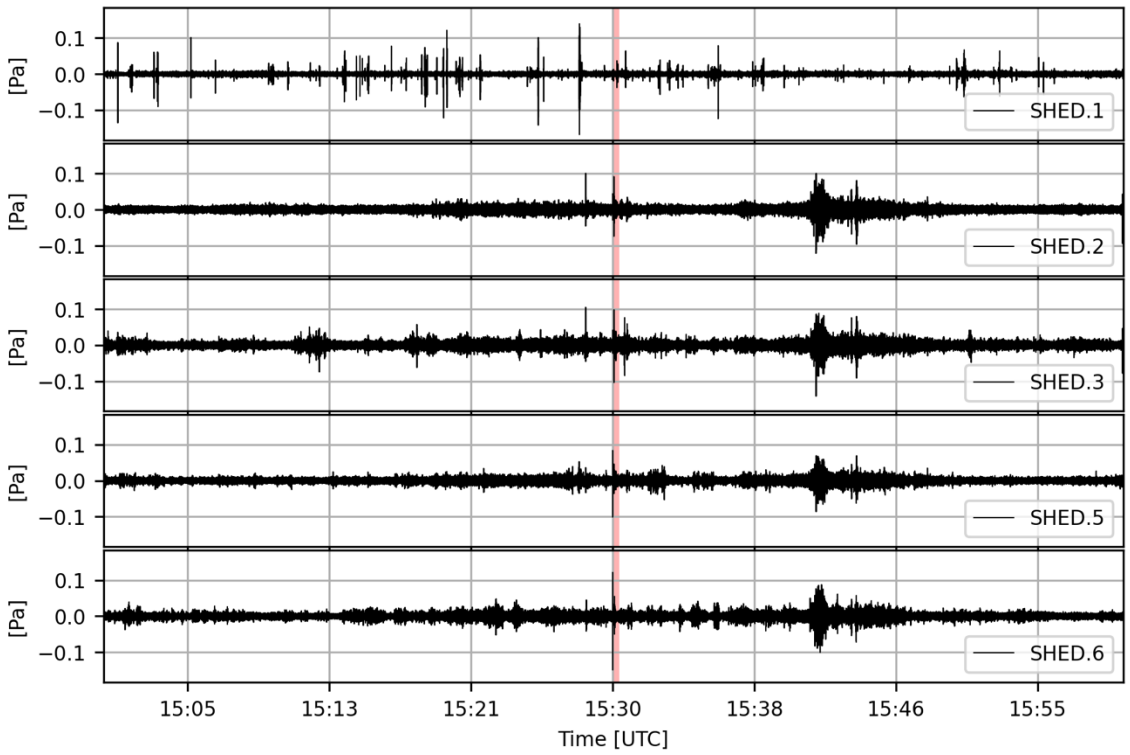

Figure 36. Waveforms highpassed above 5 Hz for SHED elements 1, 2, 3, 5, and 6. Waveforms show 30 minutes on either side of the earthquake origin time. The duration highlighted in red is the same as that shown in the previous figure.

5.6.2. Interpretation

The arrival recorded at BEZO 2, 3, and 6 and the first arrival at SHED 2, 3, and 5 occur at times consistent with the arrival of seismic waves. These are likely LIS generated by the earthquake.

The possible second arrival recorded at SHED 2, 3, and 5 is consistent in time with the arrival of EIS. It is odd that the other two instruments in the array — SHED 1 and 6 — do not appear to record this feature. This possible arrival is inconclusive and requires further investigation.

5.7. Event tx2023dafm

5.7.1. Results

An M3.0 earthquake with ID 'tx2023dafm' occurred on February 12, 2023 at 19:23:17 UTC at a depth of 4.5±1.1 km. Coherent infrasound signals were observed on eight instruments across all three arrays: BEZO 3 and 6; SHED 3, 5, and 6; and WIND 2, 3, and 4. This earthquake occurred 11.3± 1.1, 4.0± 1.1, and 4.7 ± 1.1 km from the central elements of the BEZO, SHED, and WIND arrays, respectively. As seen in Figures Figure 37, Figure **39**, and Figure **41**, each infrasound observation is comprised of ~5–40 Hz waves with amplitudes of 0.15 – 2.0 Pa. All arrivals occur just after the predicted arrival of a 3.5 km/s P-wave. The arrivals at all three arrays are relatively high SNR relative to the background noise conditions, as seen in Figures Figure **38**, Figure **40**, and Figure **42**.

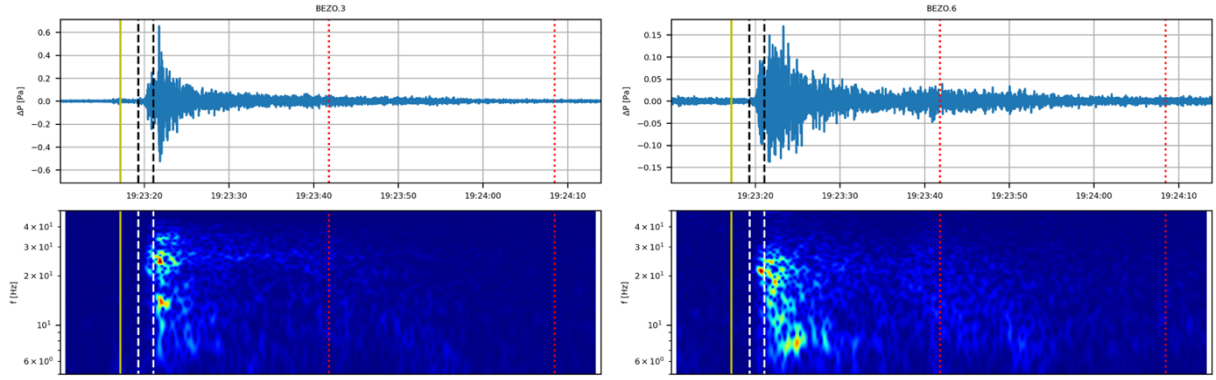

Figure 37. Waveforms and spectrograms of 5–50 Hz bandpassed infrasound recordings at instruments at BEZO elements 3 and 6.

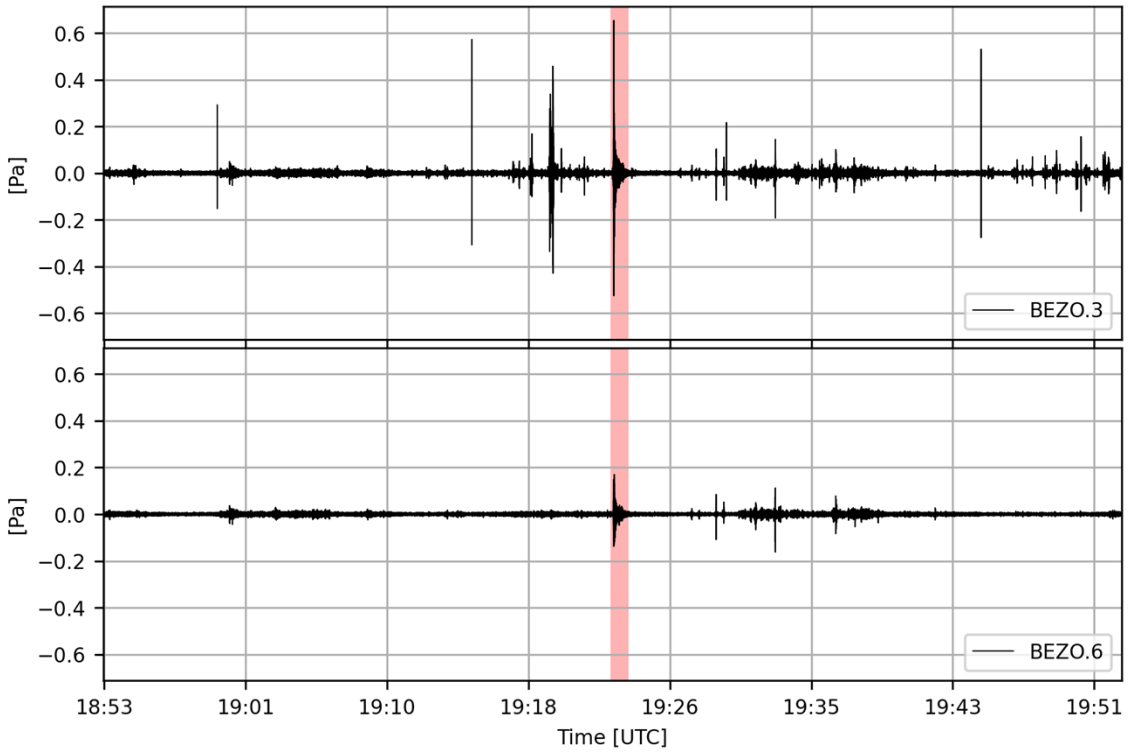

Figure 38. Waveforms highpassed above 5 Hz for BEZO elements 3 and 6. Waveforms show 30 minutes on either side of the earthquake origin time. The duration highlighted in red is the same as that shown in the previous figure.

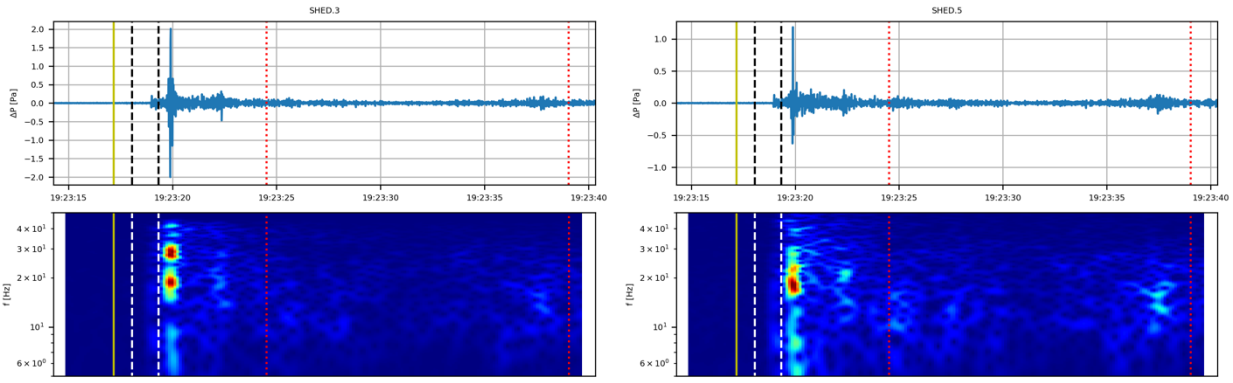

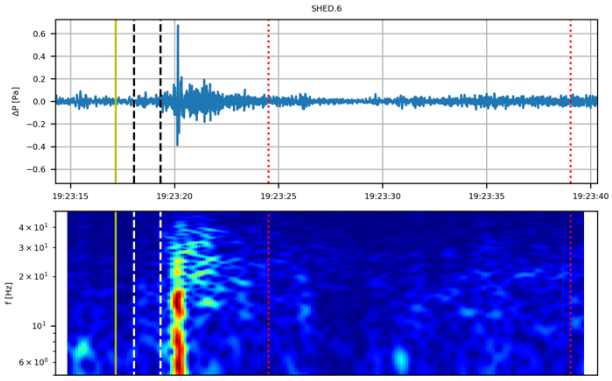

Figure 39. Waveforms and spectrograms of 5–50 Hz bandpassed infrasound recordings at SHED elements 3, 5, and 6.

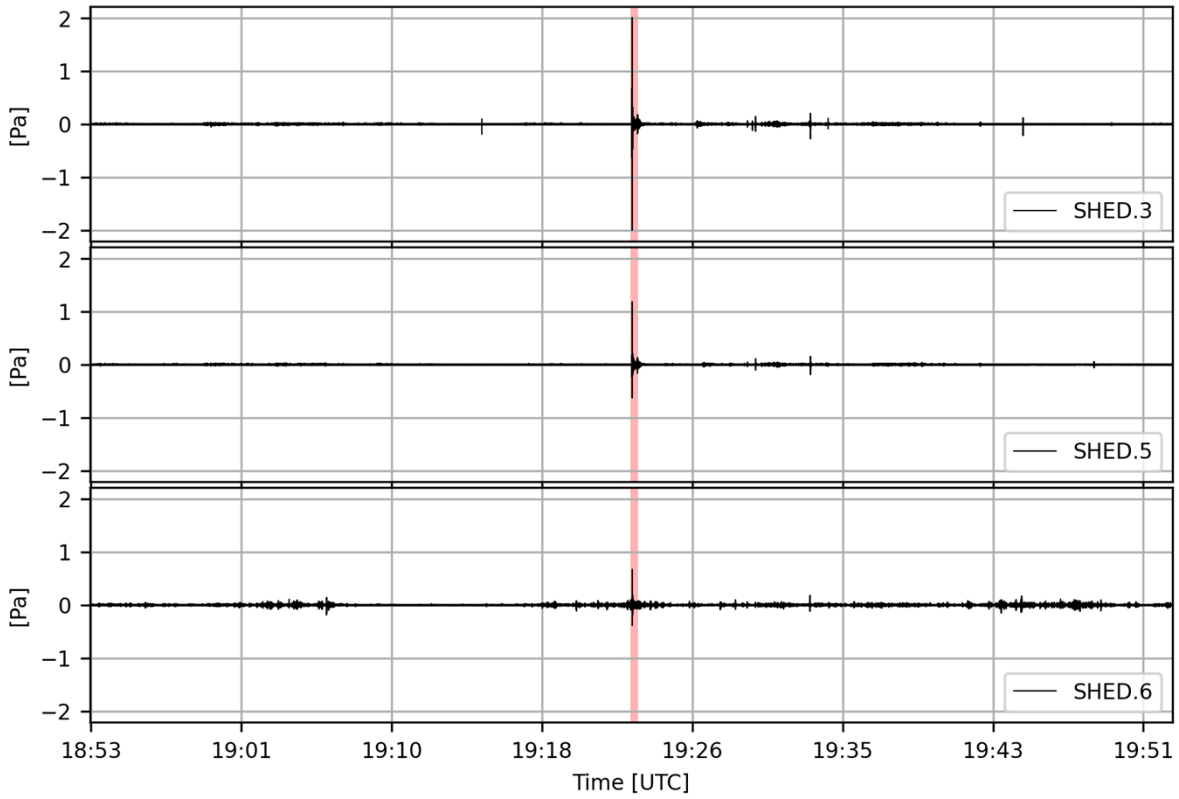

Figure 40. Waveforms highpassed above 5 Hz for SHED elements 3, 5, and 6. Waveforms show 30 minutes on either side of the earthquake origin time. The duration highlighted in red is the same as that shown in the previous figure.

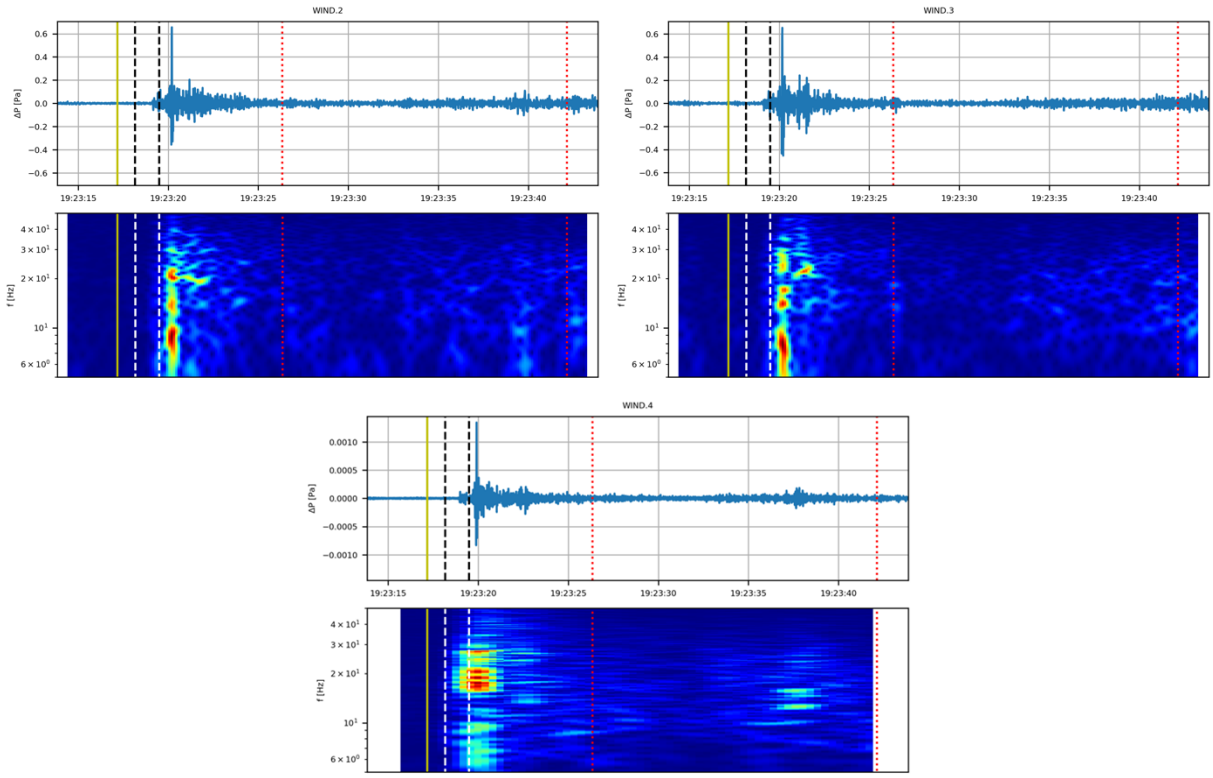

Figure 41. Waveforms and spectrograms of 5–50 Hz bandpassed infrasound recordings at WIND elements 2, 3, and 4. The absolute values of amplitudes recorded on element 4 are inaccurate and therefore only relative amplitudes are considered.

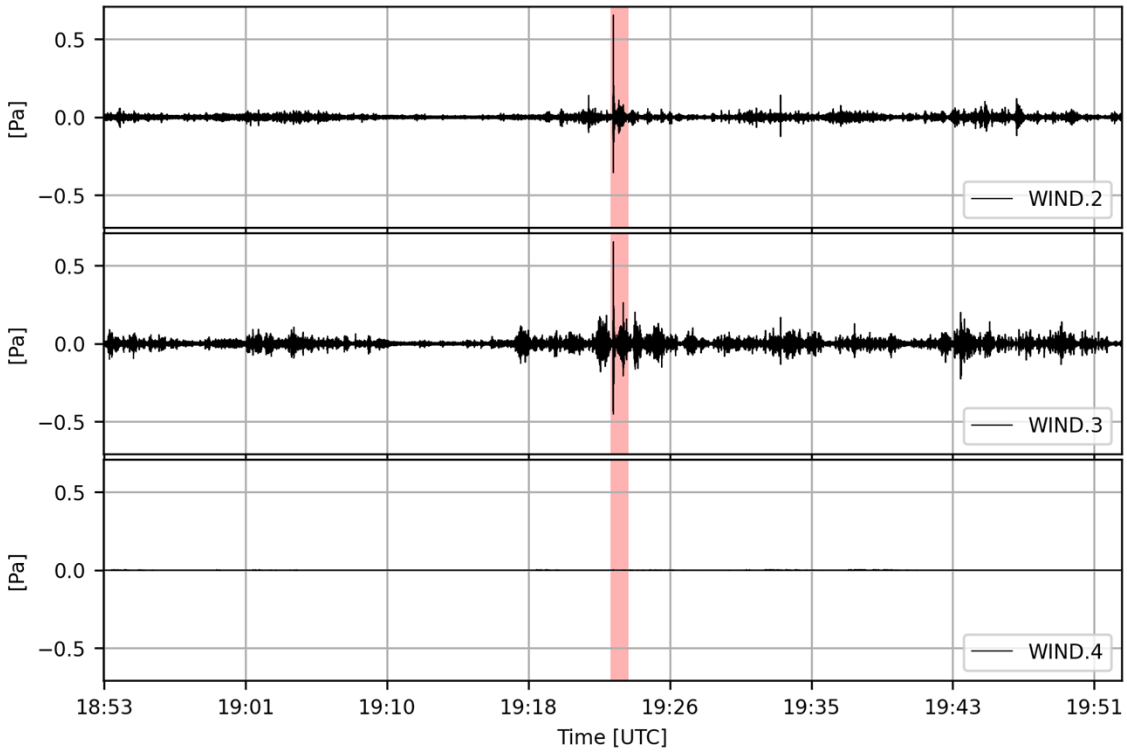

Figure 42. Waveforms highpassed above 5 Hz for WIND elements 2, 3, and 4. Waveforms show 30 minutes on either side of the earthquake origin time. The duration highlighted in red is the same as that shown in the previous figure. The absolute values of amplitudes recorded on element 4 are inaccurate and therefore display near zero.

5.7.2. Interpretation

Instruments at all three arrays record a high SNR, broadband feature that begins in the window of expected seismic arrivals. The waveform and spectrograms are most similar for elements at SHED and WIND, which are 4.0 and 4.7 km away, respectively, compared to BEZO, which is 11.3 km away from the event. The amplitudes of this feature are lower for the seismically decoupled sensors than those that are not, further suggesting that this feature is LIS caused by seismic movement of the instrument.

There is a possible second arrival recorded on SHED 3 and 5 around 19:23:38 and on WIND 2 and 4 around 19:23:40 and 19:23:37, respectively. This possible arrival is near the end of the predicted EIS window and has an amplitude of ~0.1–0.2 Pa on SHED 3 and 5 and WIND 2. (The absolute values of the amplitudes of WIND 4 are incorrect due a calibration error and thus only relative amplitudes are considered.)

This possible signal arrives at SHED 3 and 5 approximately two seconds before arriving at WIND 2, which is 0.7 km farther from the epicenter. The celerity of such a wavefront is within infrasonic range. This suggests that the feature may be caused by EIS. This interpretation is complicated however, when considering the arrival of this feature at WIND 4, which is approximately one second before the arrival at SHED, which is closer to the event. We have one recording at WIND that is consistent with EIS and one that is not, leaving this feature currently inconclusive but deserving of further consideration.

5.8. Event tx2023dvvu

5.8.1. Results

An M2.7 earthquake with ID 'tx2023dvvu' occurred on February 24, 2023, at 15:28:00 UTC at a depth of 5.7±1.3 km. Similar infrasound signals were observed on SHED elements 3, 5, and 6 and WIND elements 2 and 3. The earthquake occurred 3.6±1.0 and 2.0 ±1.0 km from the centers of the SHED and WIND arrays, respectively. There are possibly two arrivals, as seen in Figures Figure **43**Figure 45. The first arrival is most obvious, occurring near the predicted arrival of a 3.5 km/s P-wave on all 5 elements here. This arrival is comprised of ~5–30 Hz waves with amplitudes of 0.04–0.1 Pa. As seen in Figure 44Figure 46, these signals are of similar amplitude to the prevailing noise conditions.

SHED 3, 5, and 6 all record a ~9–12 Hz feature near the end of the predicted EIS window. WIND 2 and 3 also record a ~7–9 Hz feature near the end of the EIS window.

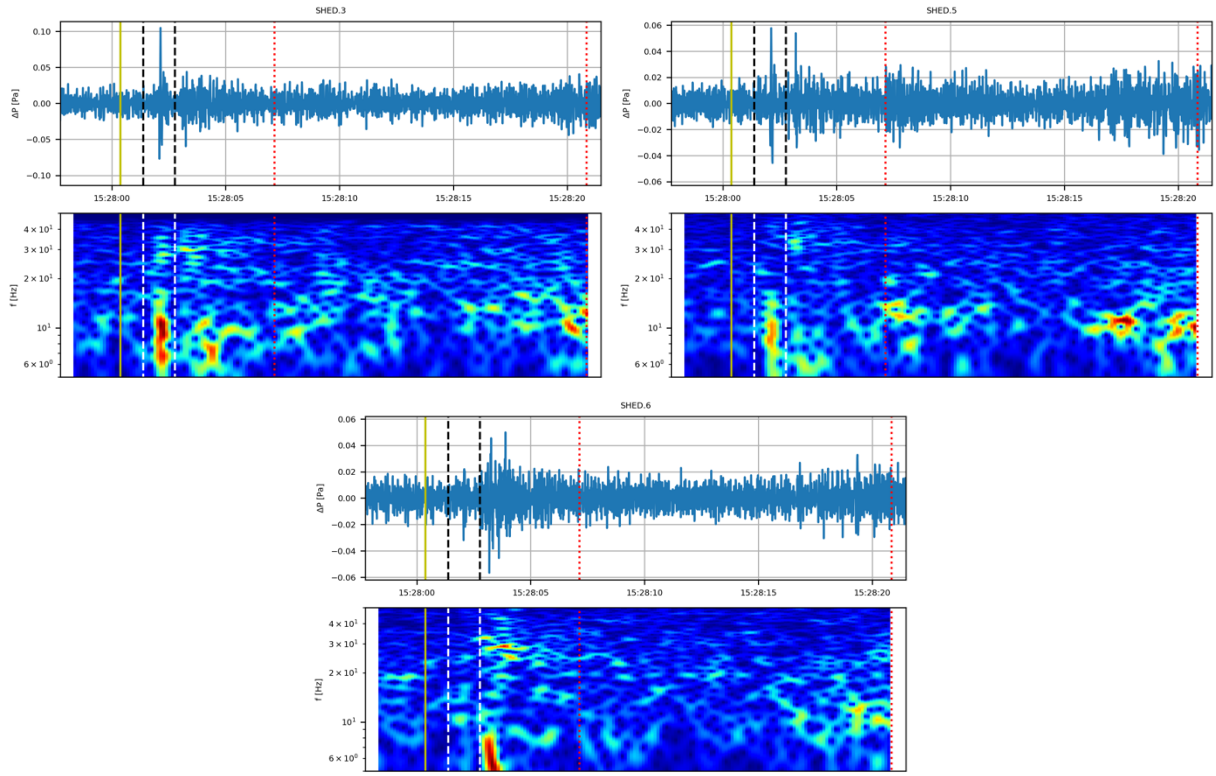

Figure 43. Waveforms and spectrograms of 5–50 Hz bandpassed infrasound recordings at SHED elements 3, 5, and 6.

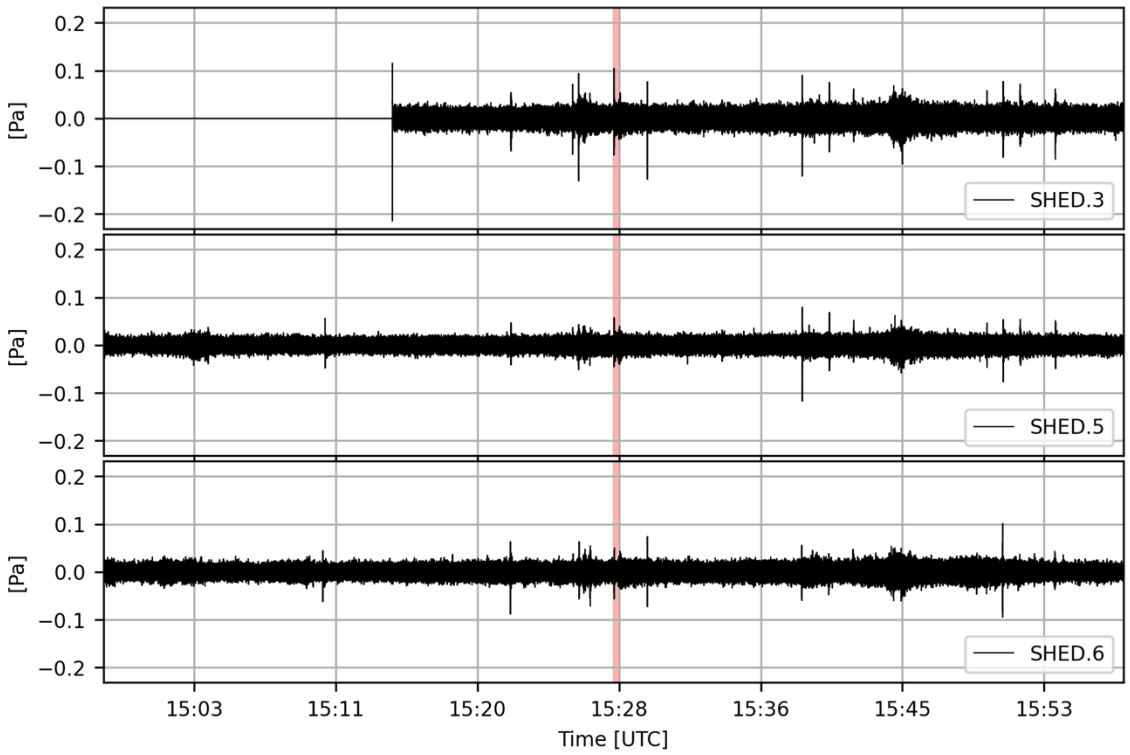

Figure 44. Waveforms highpassed above 5 Hz for SHED elements 3, 5, and 6. Waveforms show 30 minutes on either side of the earthquake origin time. The duration highlighted in red is the same as that shown in the previous figure.

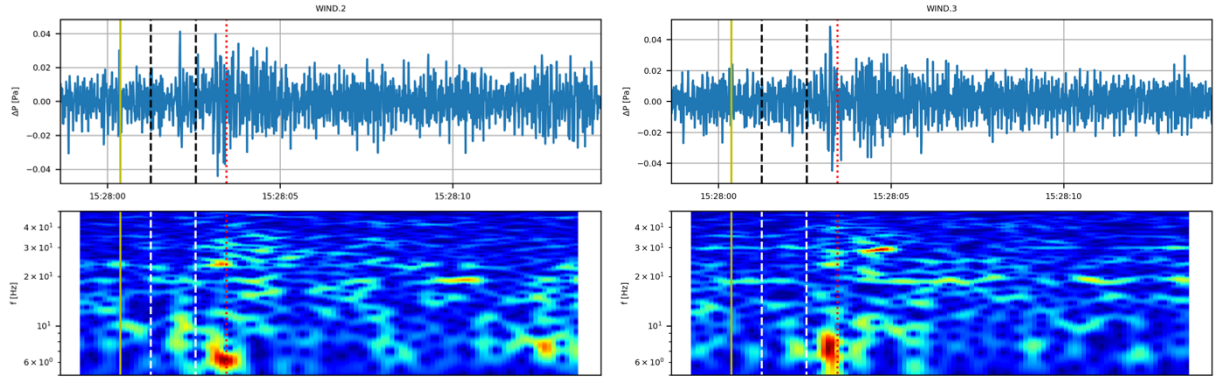

Figure 45. Waveforms and spectrograms of 5–50 Hz bandpassed infrasound recordings at WIND elements 2 and 3.

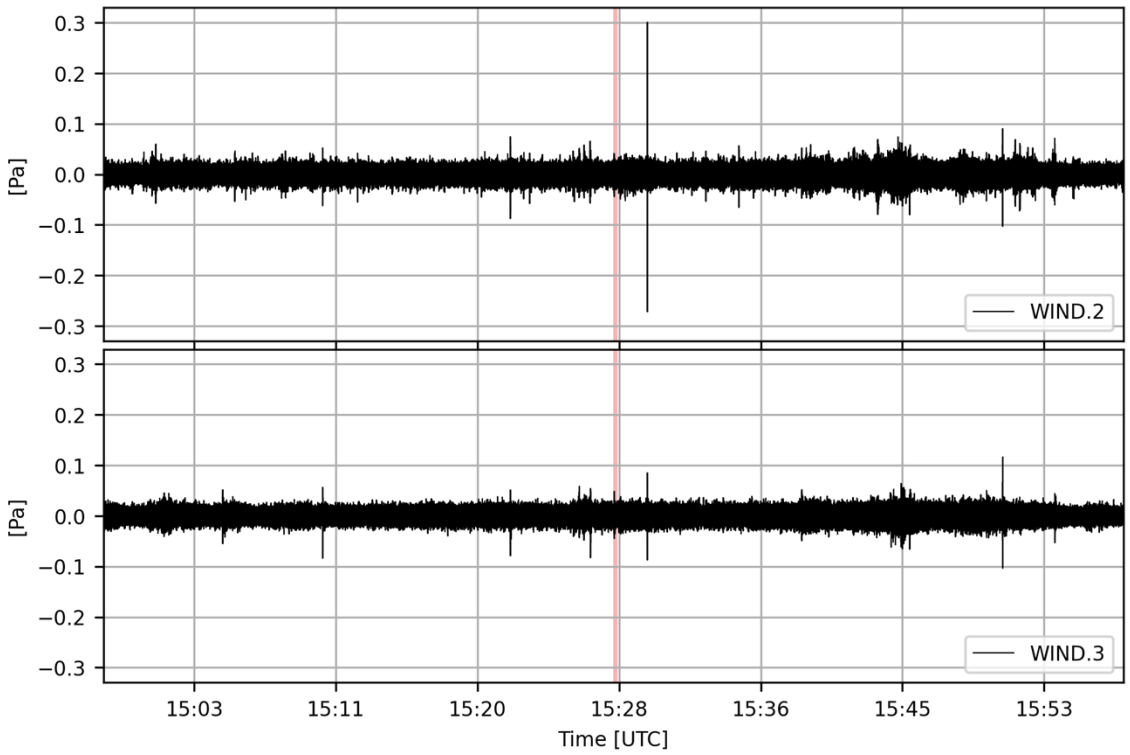

Figure 46. Waveforms highpassed above 5 Hz for WIND elements 2 and 3. Waveforms show 30 minutes on either side of the earthquake origin time. The duration highlighted in red is the same as that shown in the previous figure.

5.8.2. Interpretation

The first arrival is consistent with the arrival of seismic waves and is therefore likely LIS. The possible second arrival appears consistent with EIS but needs further consideration. Caution is needed because all suspected arrivals have low SNR. Interpretation is further complicated because WIND is within the epicentral, only 2.0±1.1 km from the epicenter. As such, LIS would be a recording of the epicentral motion and EIS could be generated near or at the same location as the instrument.

6. DISCUSSION

6.1. Infrasound Detections

Table 3 summarizes the infrasound signals detected and their interpretations. We find infrasound signals associated with eight of the 84 events considered. We observe LIS arrivals associated with all but one of the eight events described here. Such arrivals of LIS are broadband excitations of frequencies between 5–40 Hz. Most LIS arrivals occur just after the predicted window of a 3.5 km/s P-wave, though some occur within it (as in tx2023dvvu). Amplitudes vary from 0.08 (events tx2023cdzu, SHED 2) to 2.0 Pa (event tx2023dafm, SHED 3).

Seven events also had later arrivals that were considered as possible EIS. These arrivals were generally comprised of a narrow band of frequencies than the earlier arrivals (i.e. 1–20 Hz rather than 5–40 Hz). The amplitudes of these arrivals were also generally less than the earlier arrivals, though with exceptions (tx2023bvwo).

The eight events had magnitudes from 2.5 (the lowest value considered in this study) to 3.0. LIS was detected at distances of 2.7 (event tx2023cauk, SHED) to 38.3 km (event tx2023bvwo, BEZO).

Table 3. Summary of arrivals observed following each of the eight events

Event		Earlier arrival			Later arrival			
ID	MAG	f [Hz]	Amp [Pa]	Interpretation	f [Hz]	Celerity [km/s]	Amp [Pa]	Interpretation
tx2023blmu	2.5	7–40 Hz	0.4–1.0	LIS	—	—	—	—
tx2023bvwo	2.9	5–30 Hz	0.015–0.04	LIS	5–30 Hz	0.535	0.02–0.06	not from EQ
tx2023cauk	2.7	6–40 Hz	0.08–0.8	LIS	8–20 Hz	0.380	0.005–0.02	possible EIS
tx2023cayr	2.9	5–40 Hz	0.15–0.6	LIS	7–15 Hz	0.390, 0.340	0.1–0.3	probable EIS
tx2023cbwa	2.5	—	—	—	15–40 Hz	0.435, 0.300	0.02–0.08	not from EQ
tx2023cdzu	2.5	6–40 Hz	0.08–0.1	LIS	10–20 Hz	0.400	0.01–0.04	possible EIS
tx2023dafm	3	5–40 Hz	0.4–2.0	LIS	10–20 Hz	—	0.1–0.2	possible EIS
tx2023dvvu	2.7	5–30 Hz	0.04–0.1	LIS	5–20 Hz	—	0.02–0.05	possible EIS

The later arrival following tx2023cayr is the best candidate for interpretation as EIS. This arrival was composed of 7–15 Hz energy with amplitudes of 0.1–0.3 Pa. Elements at SHED and WIND capture this arrival with celerities of approximately 0.390 and 0.340 km/s, respectively. Array processing of the 10–12 Hz portion of the arrival at SHED elements 2, 3, and 5 further suggests that this signal crossed the array at a velocity of 0.333–0.4 km/s. Array processing also calculates this 10–12 Hz wave as originating from a direction of ~100–110°, while the true back-azimuth is ~115°.

Johnson *et al.* (2020) observed EIS associated with two separate M3.6 events. No publications report observing EIS originating from events with magnitudes below 3.6. Event tx2023cayr was an M2.9 event. If it generated EIS that was recorded on SHED, this event will be the lowest-magnitude earthquake to have produced observed EIS. Johnson *et al.* (2020) made their observations on instruments within 25 km of the epicenter. The SHED array is 2.8 km from the epicenter and if the arrival is indeed EIS, this observation may help inform the relationship between

detection distance and event magnitude. This suspected arrival at SHED needs to be studied further to confirm or disconfirm it as an EIS wave.

6.2. Comparison of events tx2023cauk and tx2023cayr

Events tx2023cauk and tx2023cayr are nearly identical. Their epicenters are 0.18 km apart and they are of nearly the same magnitude: tx2023cauk is M2.7 and tx2023cayr is M2.9. The events occurred on the same day, less than 2 hours apart. They are also of similar depths, at 6.1 and 4.5 km, respectively. These events allow for a unique opportunity to record the same earthquake twice. The recordings look very similar between the events, supporting the interpretation that these signals were generated by the earthquake (Figures Figure 47Figure 48).

As discussed in the previous two sections, the arrivals at BEZO and the first arrivals at SHED are interpreted as LIS for both events. The remarkable similarity of the waveforms between events is worthy of further study.

The second arrival at SHED following event tx2023cauk is consistent in time with an EIS arrival but the array processing results suggest a wavefront propagation velocity >1 km/s, with an arrival from a back-azimuth of approximately -100° (Figure 19). As discussed previously, if the array processing result is true, this arrival must not be associated with the event. The second arrival at SHED following event tx2023cayr, however, is consistent with a wavefront moving across the array at acoustic velocities from the same direction as the epicenter (Figure 26). The second arrival has a velocity of 0.333–0.4 km/s from ~100–110°, while the true back-azimuth is 115° In summary, the second arrival from one event appears to be seismic from a direction unassociated with the event. The other second arrival appears acoustic from the same direction as the epicenter. The events are similar in all other ways, which suggests that both arrivals must be either seismic or acoustic, not one of each. This is deserving of further study.

There is only one recording at the WIND array and only during the period following event tx2023cayr. This one recording is insightful however, in that the waveform and spectrogram look very similar to the arrivals at SHED, which is 1.6 km closer to the epicenter (Figure 49).

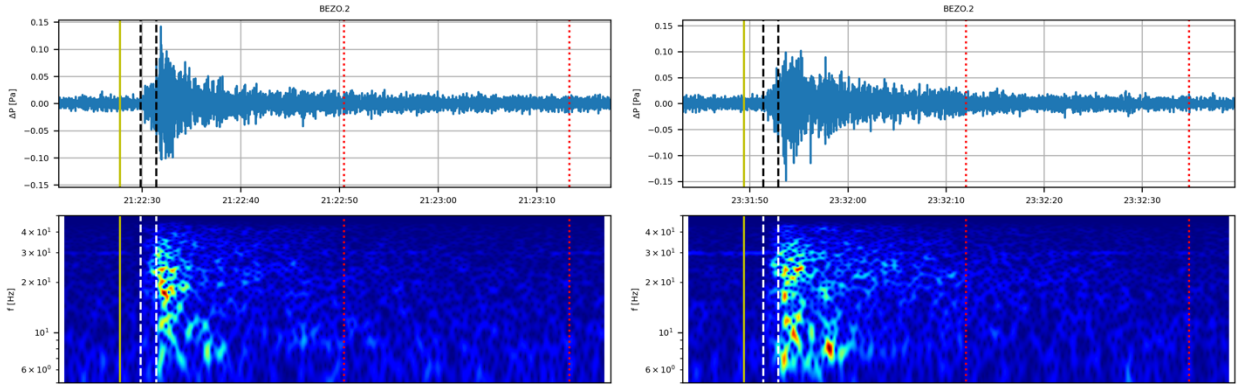

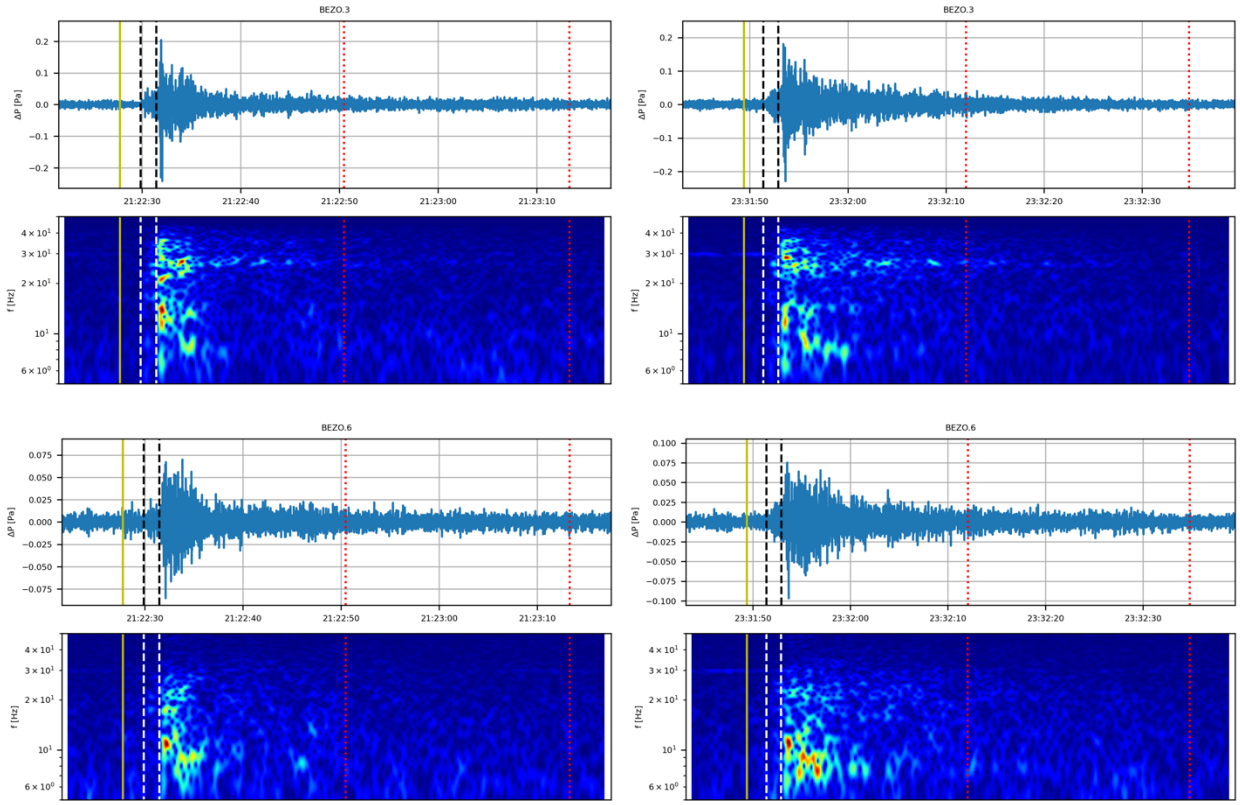

Figure 47. Comparisons of recordings at BEZO elements 2, 3, and 6 associated with events tx2023cauk (left column) and tx2023cayr (right column).

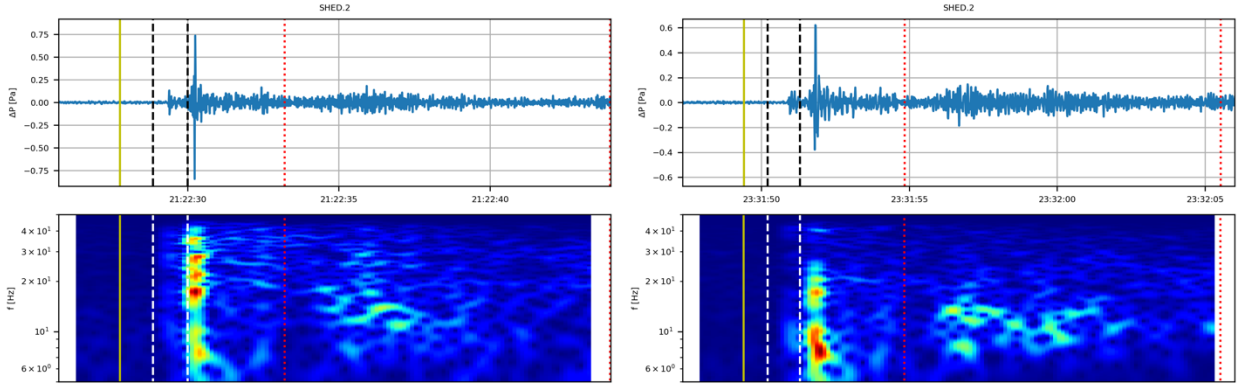

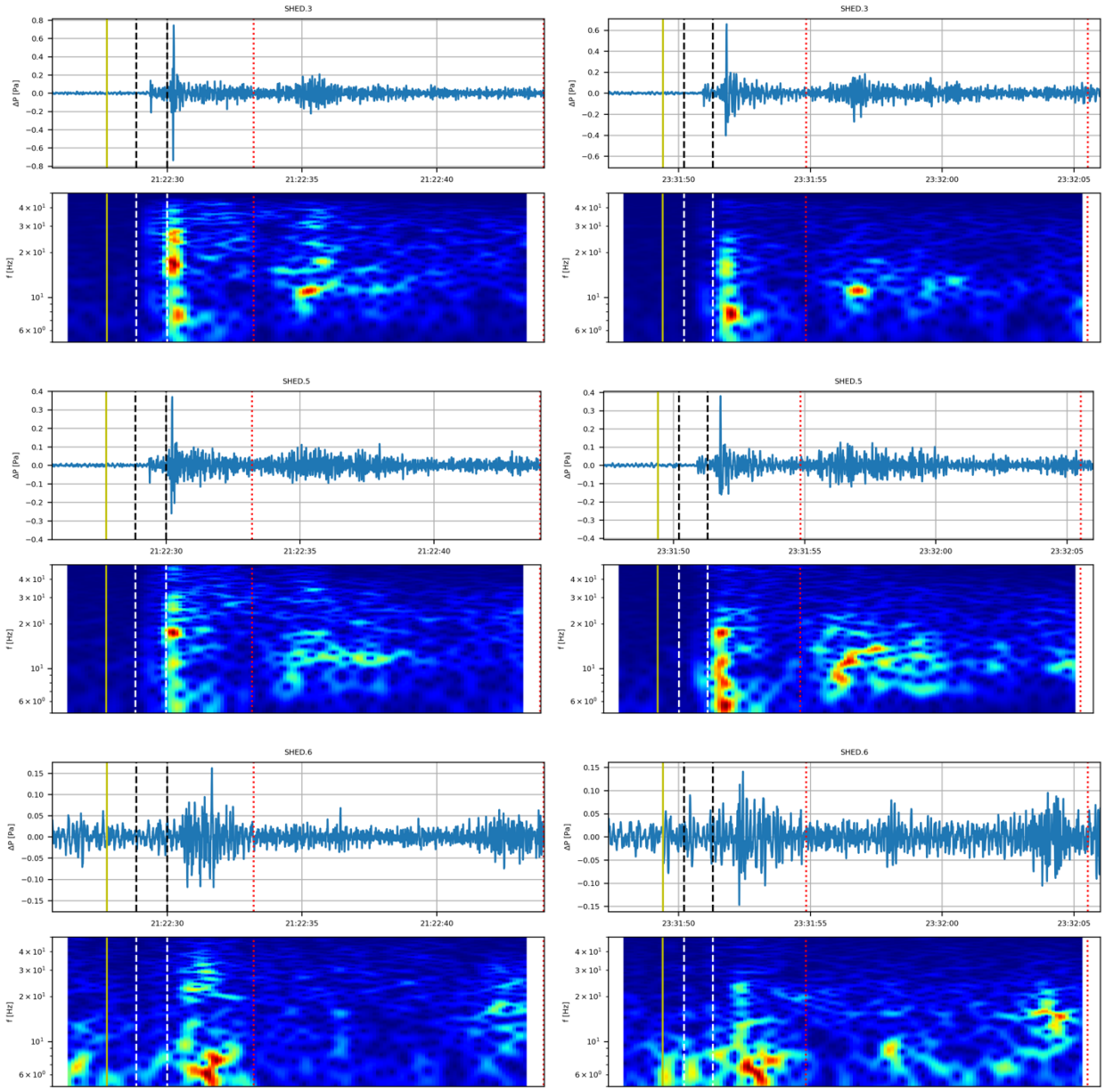

Figure 48. Comparison of recordings at SHED elements 2, 3, 5, and 6 associated with events tx2023cauk (left column) and tx2023cayr (right).

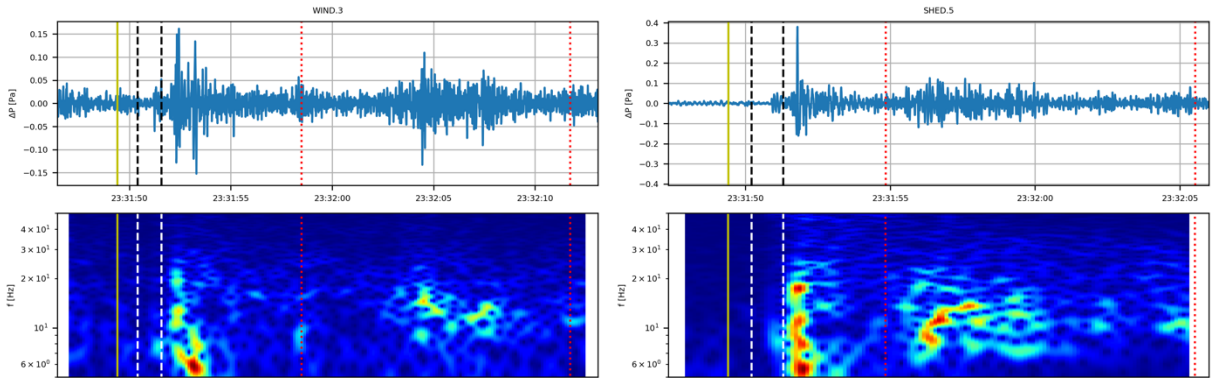

Figure 49. Comparison of signals recorded at WIND 3 and SHED 5 following event tx2023cayr.

7. CONCLUSIONS AND FUTURE WORK

Three arrays of infrasound instruments collected data in the Permian Basin from January to June of 2023. This paper overviews analysis of the infrasound data following earthquakes with M≥2.5 occurring in the earlier half of the collection period. We find infrasound signals associated with eight earthquakes. All but one of those events appears to have generated LIS signals at or near the receivers. We interpret the detection of laterally propagating EIS following the M2.9 event tx2023cayr. We suspect that several other events may have also produced EIS but further analysis is required. Two events are associated with late arrivals that were determined to not originate from the earthquake. In summary, we find strong evidence of an M2.9 earthquake generating laterally propagating EIS.

We propose the following future work:

- Try CLEAN beamforming: CLEAN beamforming is an array processing technique (Högbom, 1974; den Ouden *et al.,* 2020). It was used to study the 2–25 Hz and 1–20 Hz infrasound originating at local M3.5 (0.6 km) and regional M6.5 (720 km) earthquakes, respectively (Johnson *et al.,* 2023). Broadband infrasound waves in this frequency range are non-dispersive but will have a common slowness vector despite having a range of wavenumber vectors (Johnson *et al.,* 2023). This technique may be useful in helping to identify the distinct wavefields that comprise suspected EIS arrivals.

- Incorporate seismic data: WIND element 3 and SHED element 6 were co–located with TexNet seismic stations PB36 and PB35, respectively. The seismic data recorded at these stations may be helpful in corroborating suspected LIS arrivals and understanding the effect of seismic decoupling of the digital instruments.

- Apply same methods to data collected in the latter half of the campaign. Data were not ready in time for these analyses. Also consider searching for infrasound arrivals associated with earthquakes with magnitudes <2.5. All the analyses here were restricted to events with magnitudes ≥2.5 under the assumption that the most energetic events would also be the most likely to generate detectable signals. Lamb *et al.* (2021) recorded LIS originating from an M1.87 event. The hypocenter was 6.3 km deep and the LIS signal was recorded on two arrays <3.5 km from the epicenter. This event created enough acoustic energy such that it was reportedly heard by people up to 9 km away (Lamb *et al.,* 2021). Our catalog includes many events with magnitudes less than M2.5 at similar depths and thus presents an opportunity to study even less energetic events.

- Calculate the array response function for each of the arrays and sub-arrays comprised of a subset of the elements, as in Wilson *et al.* (2023). The array response function will inform the capacity of each array and sub-array to resolve back-azimuths and wavefront propagation velocities. Such information could help hone the array processing method and the interpretation of the results.

REFERENCES

Arrowsmith, S. J., Johnson, J. B., Drob, D. P., & Hedlin, M. A. (2010). The seismoacoustic wavefield: A new paradigm in studying geophysical phenomena. *Reviews of Geophysics*, 48(4).

Arrowsmith, S. J., Burlacu, R., Pankow, K., Stump, B., Stead, R., Whitaker, R., and Hayward, C. (2012). A seismoacoustic study of the 2011 January 3 Circleville earthquake, *Geophys. J. Int.* doi: 10.1111/j.1365-246X.2012.05420.x.

Beyreuther, M., Barsch, R., Krischer, L., Megies, T., Behr, Y., & Wassermann, J. (2010). ObsPy: A Python toolbox for seismology. *Seismological Research Letters*, 81(3), 530-533.
Bolt, B. A., Seismic air waves from the great 1964 Alaskan earthquake, *Nature,* 202, 1095–1096, 1964.

Bowman, J. R., Baker, G. E., & Bahavar, M. (2005). Ambient infrasound noise. *Geophysical Research Letters, 32*, L09803. https://doi.org/ 10.1029/2005gl022486.

Bowman, D. C., and S. Krishnamoorthy (2021). Infrasound from a buried chemical explosion recorded on a balloon in the lower stratosphere. *Geophys. Res. Lett.* 48, no. 21, doi: 10.1029/ 2021GL094861

Cook, R. K. (1971). Infrasound radiated during the Montana earthquake of 1959 August 18, *Geophys. J. Roy. Astron. Soc.* 26, 191–198, doi: 10.1111/j.1365-246X.1971.tb03393.x.

den Ouden, O. F. C., Assink, J. D., Smets, P. S. M., Shani-Kadmiel, S., Averbuch, G., and Evers L. G. (2020). CLEAN beamforming for the enhanced detection of multiple infrasonic sources. *Geophysical Journal International*, 221:1, 305–317, https://doi.org/10.1093/gji/ggaa010

Energy Information Administration (EIA), 2017, U.S. Crude Oil and Natural Gas Proved Reserves, Year-end 2017, *U.S. Energy Information Administration report.*

Energy Information Administration (EIA), 2020, Permian Basin Part 1, Wolfcamp, Bone Spring, Delaware Shale Plays of the Delaware Basin, Geology review, *U.S. Energy Information Administration report.*

Högbom J., 1974. Aperture synthesis with a non-regular distribution of interferometer baselines, *Astron. Astrophys. Suppl. Ser.*, 15, 417.10.1121/1.1531510

Huang, G.-C. D., Aiken, C., Savvaidis, A., Young, B., & Walter, J. (2017). Improving the velocity structure in the Delaware basin of West Texas for seismicity monitoring. *Eos Transactions AGU*, S23C-2339, https://agu.confex.com/agu/fm17/meetingapp.cgi/Paper/287401

Huang, G.-C. D., Savvaidis, A., & Walter, J. I. (2019). Mapping the 3-D Lithospheric Structure of the Greater Permian Basin in West Texas and Southeast New Mexico for Earthquake Monitoring. *Journal of Geophysical Research: Solid Earth, 124*. https://doi.org/10.1029/2019JB018351

Hyperion Technology Group, Inc. (2021). IFS System Overview v1.0.1*,* IFSN-52xx Infrasound Sensor Manual. Version 1.0.5

Johnson, J. B., Mikesell, T. D., Anderson, J. F., & Liberty, L. M. (2020). Mapping the sources of proximal earthquake infrasound. *Geophysical Research Letters,* 47, e2020GL091421. https://doi.org/10.1029/2020GL091421.

Johnson, J., Mikesell, T., Liberty, L., Anderson, J. (2023), Remotely imaging seismic ground shaking via large-N infrasound beamforming. *Research Square*. DOI: 10.21203/rs.3.rs-2929306/v1. Unpublished.

Koch, K. and Pilger, C. (2019). Infrasound observations from the site of past underground nuclear explosions in North Korea. *Geophysical Journal International*, 216 (1): 182-200, https://doi.org/10.1093/gji/ggy381

Lamb, O. D., J. M. Lees, P. E. Malin, and T. Saarno (2021). Audible acoustics from low-magnitude fluid-induced earthquakes in Finland, *Sci. Rep.* 11, no. 1, 1–8, doi: 10.1038/s41598-021-98701-6.

Laštovička, J., Baše, J., Hruska, F., Chum, J., Šindelářová, T., Horalek, J., Zedník, J., Krasnov, V., 2010a. Simultaneous infrasonic, seismic, magnetic and ionospheric observations in an earthquake epicentre. *J. Atmos. Terr. Phys.* 72 (16), 1231–1240. https://doi.org/10.1016/j.jastp.2010.08.005.

Le Pichon, A., Mialle, P., Guilbert, J. and Vergoz, J. (2006), Multistation infrasonic observations of the Chilean earthquake of 2005 June 13. *Geophysical Journal International*, 167: 838-844. https://doi.org/10.1111/j.1365-246X.2006.03190.x

Lomax, A., & Savvaidis, A. (2019). Improving absolute earthquake location in west Texas using probabilistic, proxy ground-truth station corrections. *Journal of Geophysical Research: Solid Earth, 124*, 11,447–11,465. https://doi.org/10.1029/ 2019JB017727

Mutschlecner, J. P., & Whitaker, R.W. (2005). Infrasound from earthquakes. *Journal of Geophysical Research, 110*, D01108. doi:10.1029/2004JD005067

Negraru, P. T., Golden, P., & Herrin, E. T. (2010). Infrasound propagation in the "Zone of Silence". *Seismological Research Letters*, 81(4), 614-624.

Savvaidis, A., Young, B., Huang, G.-C. D., & Lomax, A. (2019). TexNet: A statewide seismological network in Texas. *Seismological Research Letters*. https://doi.org/10.1785/0220180350

Sylvander, M., Ponsolles, C., Benahmed, S. & Fels, J. F (2007). Seismoacoustic recordings of small earthquakes in the Pyrenees: Experimental results. *Bull. Seismol. Soc. Am. 97*, 294–304. https://doi.org/10.1785/0120060009

Walker, K. T., Shelby, R., Hedlin, M. A. H., de Groot-Hedlin, C., and Vernon, F. (2011). Western U.S. Infrasonic Catalog: Illuminating infrasonic hot spots with the USArray. *J. Geophys. Res.*, 116, B12305. doi:10.1029/2011JB008579

Whitaker, R. W., Sandoval, T. D. and Mutschlecner, J. P. (2003). Recent infrasound analysis, in Proc. of the 25th Seismic Research Review-Nuclear Explosion Monitoring: Building the Knowledge Base, National Nuclear Security Administration, Washington, D.C., 646–654.

Wilson, T. C., Danneman Dugick, F.K., Bowman, D.C., Petrin, C.E., and Elbing, B.R. (2023). Seismoacoustic Signatures Observed During a Long-Term Deployment of Infrasound Sensors at the Nevada National Security Site, *Bull. Seismol. Soc. Am.* XX, 1–20, doi: 10.1785/0120220240.

DISTRIBUTION

Email—Internal

Name	Org.	Sandia Email Address
Daniel Bowman	06752	dbowma@sandia.gov
Fransiska Dannemann Dugick	06752	fkdanne@sandia.gov
Loring Schaible	06752	dpschai@sandia.gov
Technical Library	1911	sanddocs@sandia.gov

Sandia National Laboratories

Sandia National Laboratories is a multimission laboratory managed and operated by National Technology & Engineering Solutions of Sandia LLC, a wholly owned subsidiary of Honeywell International Inc. for the U.S. Department of Energy's National Nuclear Security Administration under contract DE-NA0003525.